PAPER

Striations in moderate pressure dc driven nitrogen glow discharge

IOP Publishing Journal of Physics D: Applied Physics

J. Phys. D: Appl. Phys. **55** (2022) 085201 (18pp) https://doi.org/10.1088/1361-6463/ac33da

Striations in moderate pressure dc driven nitrogen glow discharge

Malik M Tahiyat[1], Jacob C Stephens[2], Vladimir I Kolobov[3] and Tanvir I Farouk[1,*]

[1] Department of Mechanical Engineering, University of South Carolina, Columbia, SC 29208, United States of America
[2] Department of Electrical and Computer Engineering, Texas Tech University, Lubbock, TX, 79409, United States of America
[3] University of Alabama in Huntsville, Huntsville, AL, Huntsville, AL 35806, United States of America

E-mail: tfarouk@sc.edu

Received 6 August 2021, revised 17 October 2021
Accepted for publication 27 October 2021
Published 15 November 2021

Abstract

Plasma stratification has been studied for more than a century. Despite the many experimental studies reported on this topic, theoretical analyses and numerical modeling of this phenomenon have been mostly limited to rare gases. In this work, a one-dimensional fluid model with detailed kinetics of electrons and vibrationally excited molecules is employed to simulate moderate-pressure (i.e. a few Torrs) dc discharge in nitrogen in a 15.5 cm long tube of radius 0.55 cm. The model also considers ambipolar diffusion to account for the radial loss of ions and electrons to the wall. The proposed model predicts self-excited standing striations in nitrogen for a range of discharge currents. The impact of electron transport parameters and reaction rates obtained from a solution of local two-term and a multi-term Boltzmann equation on the predictions are assessed. In-depth kinetic analysis indicates that the striations result from the undulations in electron temperature caused due to the interaction between ionization and vibrational reactions. Furthermore, the vibrationally excited molecules associated with the lower energy levels are found to influence nitrogen plasma stratification and the striation pattern strongly. A balance between ionization processes and electron energy transport allows the formation of the observed standing striations. Simulations were conducted for a range of discharge current densities from ∼0.018 to 0.080 mA cm^{-2}, for an operating pressure of 0.7 Torr. Parametric studies show that the striation length decreases with increasing discharge current. The predictions from the model are compared against experimental measurements and are found to agree favorably.

Keywords: diatomic gas, striations, vibrational-excitation, glow discharge, electron energy distribution

(Some figures may appear in colour only in the online journal)

1. Introduction

The self-organized formation of spatial light emission patterns has been a research topic due to its impact on various plasma systems operating in low to atmospheric pressure range, with either a dc or rf source for a wide range of discharge parameters [1–3]. Alternating bright and dark areas along the discharge current are usually termed 'stratification'. Two types of striations have been observed: 'standing' striations in the form of stationary damping oscillations in the vicinity of electrodes and 'moving' striations with speeds in the order of 10–10^3 ms^{-1} [4]. Striations have been observed at low and high gas pressures in dc and rf discharges [5–9]. One of the most commonly studied, is the striated positive column of a dc glow discharge, where ionization waves or ion-acoustic waves drive the observed phenomenon [2, 10]. Plasma stratification in dc discharges was studied extensively in the past

* Author to whom any correspondence should be addressed.

[11, 12] for low and moderate pressures, at $PR < 10$ Torr cm (P is operating pressure and R is the discharge tube radius). In recent years, studies have been conducted for high-pressure micro discharges at PR up to ∼25 Torr cm [8]. Fluid [13, 14] and kinetic models [2, 5, 9, 15, 16] have been developed to simulate plasma stratification. A comprehensive review of instabilities in molecular and electronegative plasmas by Haas [14] emphasized the importance of negative ions on the formation of the striated structures. Nighan and Wiegand [13] demonstrated conditions when electron-attachment processes forming negative ions trigger plasma stratification. Recent studies considering kinetic effects [15, 17] have predicted moving striations for atomic gases without negative ions.

Arslanbekov and Kolobov [15] conducted two-dimensional simulations of an argon dc glow discharge operating at moderate pressure (2 Torr) and high currents (∼100 mA). The model predicted the formation of moving striations near the Pupp boundary resulting from nonlinear dependence of the ionization and excitation rates on electron density caused by 'Maxwellization' of the high-energy part of the electron energy distribution function (EEDF). In a recent study, the same authors [18] have demonstrated the influence of volume recombination on the striation patterns at higher gas pressures. Kawamura *et al* [9] conducted particle in cell (PIC) simulations of an atmospheric pressure dc and rf discharges in helium with trace water vapor (He/H_2O). They found that volume recombination and nonlocal effects can trigger plasma stratification.

Recently, Desangles *et al* [19] have studied striations in argon rf discharge using an electron fluid model with a 0-D Boltzmann solver for the EEDF. They predicted stratification driven by Soret and Dufour effects for electron and electron energy transport. In earlier work, Urbankova and Rohlena [20] conducted a similar analysis. They identified that for moderate/low-pressure dc discharge operating in a diatomic gas, the thermal diffusion of electrons plays the most critical role in triggering standing striations. Computational studies of striations in low-pressure rf argon plasma was conducted by Hjalmar *et al* [21]; however, no discerning factor for the stratification was identified. Analysis of striations in capacitively coupled rf plasma for CF_4 gas was conducted by Liu *et al* [5]; the authors attributed the formation of the striations to the local space charge formed from the periodic acceleration of ions by the rf electric field [5]. Iza *et al* [22] conducted two-dimensional PIC simulations of plasma display panels, where striations were formed due to a combined effect of volume processes and surface charge accumulation. In magnetized microdischarges, striations have also been observed [23]. Numerical studies of the non-local electron kinetics leading to plasma stratification have been reported in the literature [24–26]. In a recent study, Levko [27] observed standing and moving striations in low-pressure dc and rf argon discharges using one-dimensional PIC simulations; however, no mechanism of stratification has been identified.

Despite many theoretical and modeling studies of plasma stratification in several gases, modeling striations in diatomic gases has been limited. Sigeneger *et al* [28] attempted to study the non-local electron kinetics in spherical glow discharges in nitrogen (N_2) by solving a spatially inhomogeneous Boltzmann equation (BE) for a given distribution of the electric field. No self-consistent numerical modeling of striations in diatomic gases has been performed so far.

This work describes a one-dimensional model to simulate low/moderate pressure dc glow discharge in nitrogen. A detailed chemistry model is assembled that includes elastic scattering, ionization, volumetric recombination, multi-level vibrational excitation and de-excitation, as well as electronic excitation and de-excitation. The reaction rate constants and transport coefficients of electrons have been obtained from a multi-term spherical harmonics expansion (SHE) solution of the local BE. Experiments are conducted to obtain the voltage-current characteristics and record the visual appearance of the striations.

2. Mathematical model and problem geometry

The mathematical model provides a 1D representation of the dc glow discharge resolving the temporal and spatial variations of the plasma parameters in the direction normal to the electrodes (figure 1). The discharge model consists of coupled conservation equations for the electrons, ions, and neutrals, as well as electron energy. The electric field is self consistently obtained from the solution of Poisson's equation. The cathode is grounded, and the voltage is applied to the anode through a simple RC circuit (figure 1). The capacitance, C_p represents the parasitic capacitance (0.1 pF) of the connecting wires in the circuit. The ballast resistance, R_{Ballast}, is varied to control the discharge current, hence, the plasma density. The inter-electrode separation distance (L) is 15.5 cm, and the diameter of each electrode is 1.1 cm. The resulting electrode surface area of 0.95 cm^2 is used for calculating the discharge current of the system. The standard flux boundary conditions for electrons, ions, and electron energy are prescribed. The secondary electron emission coefficient is set to $\gamma = 0.1$.

The discharge is represented as a 1.5-dimensional system. The details of all the governing equations, and boundary conditions have been reported in our prior publications [29, 30]. In this work, ambipolar losses of electron ($\frac{n_e}{\tau_d}$), ions ($\frac{n_i}{\tau_d}$) and mean electron energy ($\frac{n_e\varepsilon}{\tau_d}$) are considered, where, n is species number density, subscripts e and i denote electrons and ions respectively and ε is the mean electron energy. The ambipolar diffusion time scale is denoted by $\tau_d(x) = \frac{\Lambda^2}{D_a(x)}$, where $\Lambda = \frac{R_{\text{tube}}}{2.4}$ is the transverse discharge length (R_{tube} is the tube or discharge radius) [27, 31] and $D_a(x)$ is the ambipolar diffusion coefficient obtained from $D_a(x) = \frac{\mu_e \sum n_i D_i + D_e \sum n_i \mu_i}{n_e \mu_e + \sum n_i \mu_i}$ [32], where μ is the mobility, D is the diffusion coefficient.

The system of equations is discretized based on the finite element method and is solved using a time-dependent solver in COMSOL Multiphysics® v. 5.3a [33]. A non-uniform mesh is employed with denser grids near the electrodes to resolve the sheaths. The domain is decomposed with 400 non-uniform grids for which a grid-independent solution was achieved. The time integration is performed using a fully implicit backward

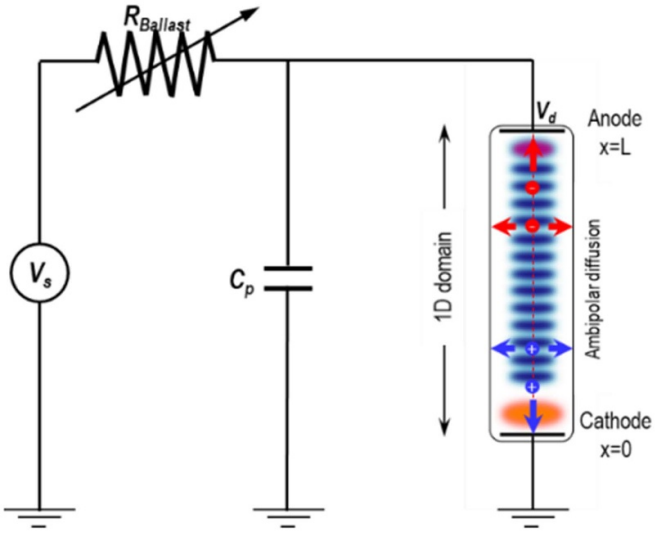

Figure 1. Schematic of the parallel plate plasma glow discharge circuit together with the 1D computational domain.

difference formula with variable time stepping. The solutions are obtained using the MUMPS (Multifrontal Massively Parallel Sparse) solver.

3. Gas phase chemical kinetics

The chemical kinetic model contains both electron induced and heavy particle reactions for nitrogen feed gas. A total of 22 species are considered, including electrons, ions, vibrational and electronically excited states, and ground-state neutrals (see table 1).

A total of 73 gas-phase reactions are considered as listed in table 2. They are grouped into two categories—electron-induced and heavy particle reactions. The electron-induced reactions include elastic scattering, vibrational excitation, electronic excitation, ionization, recombination, de-excitation reactions, as well as super elastics collisions. The heavy particle reactions include charge transfer, de-excitation, dissociation and dissociative de-excitation reactions. Wall reactions involving the deactivation of the excited species at the electrode surfaces having a sticking coefficient of 1.0 are also considered.

A large number of the reactions listed in table 2 have cross-section data; the majority of these data on excitation and ionization of the molecular N_2 is obtained from the Biagi database [34, 44], and that of atomic N from the IST-Lisbon database [35]. However, while solving the BE for the EEDF, all the electron-induced reactions on each specific species from the respective databases are considered (see appendix). The detailed subset of electron-induced reactions allows accurately resolving of the EEDF with its salient features along with the resulting rate constants and transport parameters. However, for the one-dimensional simulation, only the reactions listed in table 2 are considered to reduce the computational overhead—an approach that was adopted in prior works [45, 46]. Electron–electron collisions are ignored

Table 1. Different species considered in the dc driven nitrogen plasma model.

Electrons	e
Ions	N^+, N_2^+, N_4^+
Vibrationally excited states	$N_{2,v=1}$, $N_{2,v=2}$, $N_{2,v=3}$, $N_{2,v=4}$, $N_{2,v=5}$, $N_{2,v=6}$, $N_{2,v=7}$, $N_{2,v=8}$, $N_{2,v=9}$, $N_{2,v=10}$, $N_{2,v=11}$, $N_{2,v=12}$, $N_{2,v=13}$, $N_{2,v=14}$, $N_{2,v=15}$
Electronically excited states	N_2 $(A^3\Sigma)$
Neutrals	N, N_2

since the discharge currents in the model are in the range of milliamperes as coulomb collisions become pertinent only at very high currents.

Most of today's fluid plasma models incorporate the electron-induced reaction rates and transport coefficients from local BE solvers, which require electron-neutral cross-sections data as inputs. Both the cross-sections data and the fidelity of the BE solver influence the model predictions. The SHE in velocity space is usually truncated to the first two terms when solving the BE. Such models are referred to as two-term SHE models, while models that consider more than two spherical harmonics terms are considered multi-term models. Qualitatively, the truncation to only two spherical harmonics assumes that the velocity distribution of the electrons is close to isotropic. It is widely acknowledged that the two-term approximation is inadequate for most gases at high electron energies and high values of the reduced electric field (E/n) [47]. However, for nitrogen, the two-term SHE may be insufficient even for low-energy electrons.

Generally, gases with large inelastic cross-sections can induce highly anisotropic velocity distribution functions at low electron energies. Molecular nitrogen is an example of such a gas, with large vibrational excitation cross-sections compared to elastic cross-sections. For this reason, molecular nitrogen was the focus of several early multi-term BE studies [48, 49]. It was revealed that the electron mobility and diffusion coefficients predicted by the two-term BE models could have an error up to tens of percent. Similarly, the two-term BE models could underpredict the excitation rates of the lower electronic states by tens of percent [49]. The electron-neutral excitation cross-sections for nitrogen compiled from Biagi's Fortran code, MagBoltz, are used in a Monte-Carlo simulation and the multi-term BE code. While the limitations associated with the two-term BE models are well-known, the cascading effects introduced by the two-term approximation on the results of other models are less explored [50, 51].

This study obtains reaction rates and electron transport parameters using 'MultiBolt' [52], considering a four-term expansion to represent BE. For comparing model predictions with a truncated BE model, simulations are also performed for the reaction and transport data obtained with the 'BOLSIG+' solver [53]. Both the BE models calculate the EEDF for different values of E/n and generate the necessary reaction rate and transport parameters as lookup tables. These lookup tables are generated as a function of the mean electron energy to take

Table 2. Gas-phase reaction mechanism.

	Reaction	Reaction rate coefficient	Reference
		Electron induced reactions	
R1	$e + N_2 \rightarrow e + N_2$	$f(\varepsilon)$	[34]
R2	$e + N_2 \rightarrow e + N$	$f(\varepsilon)$	[35]
R3	$e + N_2 \rightarrow e + N_{2,v=1}$	$f(\varepsilon)$	[34]
R4	$e + N_2 \rightarrow e + N_{2,v=2}$	$f(\varepsilon)$	[34]
R5	$e + N_2 \rightarrow e + N_{2,v=3}$	$f(\varepsilon)$	[34]
R6	$e + N_2 \rightarrow e + N_{2,v=4}$	$f(\varepsilon)$	[34]
R7	$e + N_2 \rightarrow e + N_{2,v=5}$	$f(\varepsilon)$	[34]
R8	$e + N_2 \rightarrow e + N_{2,v=6}$	$f(\varepsilon)$	[34]
R9	$e + N_2 \rightarrow e + N_{2,v=7}$	$f(\varepsilon)$	[34]
R10	$e + N_2 \rightarrow e + N_{2,v=8}$	$f(\varepsilon)$	[34]
R11	$e + N_2 \rightarrow e + N_{2,v=9}$	$f(\varepsilon)$	[34]
R12	$e + N_2 \rightarrow e + N_{2,v=10}$	$f(\varepsilon)$	[34]
R13	$e + N_2 \rightarrow e + N_{2,v=11}$	$f(\varepsilon)$	[34]
R14	$e + N_2 \rightarrow e + N_{2,v=12}$	$f(\varepsilon)$	[34]
R15	$e + N_2 \rightarrow e + N_{2,v=13}$	$f(\varepsilon)$	[34]
R16	$e + N_2 \rightarrow e + N_{2,v=14}$	$f(\varepsilon)$	[34]
R17	$e + N_2 \rightarrow e + N_{2,v=15}$	$f(\varepsilon)$	[34]
R18	$e + N_2 \rightarrow e + N_2\left(A^3\Sigma\right)$	$f(\varepsilon)$	[34]
R19	$e + N_{2,v=1} \rightarrow e + N_2\left(A^3\Sigma\right)$	$f(\varepsilon)$	[36]
R20	$e + N_{2,v=1} \rightarrow e + N_2$	$f(\varepsilon)$	[36]
R21	$e + N_2\left(A^3\Sigma\right) \rightarrow e + N_{2,v=1}$	$f(\varepsilon)$	[36]
R22	$e + N_2\left(A^3\Sigma\right) \rightarrow e + N_2$	$f(\varepsilon)$	[36]
R23	$e + N_2 \rightarrow 2e + N_2^+$	$f(\varepsilon)$	[34]
R24	$e + N_{2,v=1} \rightarrow 2e + N_2^+$	$f(\varepsilon)$	[36]
R25	$e + N \rightarrow 2e + N^+$	$f(\varepsilon)$	[35]
R26	$2e + N_2^+ \rightarrow e + N_2$	$1 \times 10^{-31}\left(\frac{T_g}{T_e}\right)^{4.5}$ ж	[37]
R27	$2e + N^+ \rightarrow e + N$	$1 \times 10^{-31}\left(\frac{T_g}{T_e}\right)^{4.5}$ ж	[37]
R28	$e + N_4^+ \rightarrow 2N + N_2$	$3.13 \times 10^{-13}(T_e)^{-0.41}$	[38]
R29	$e + N_2^+ \rightarrow 2N$	$2.36 \times 10^{-14}(T_e)^{-0.51}$	[39]
		Heavy particle reactions	
R30	$N_2^+ + 2N_2 \rightarrow N_2 + N_4^+$	1.90×10^{-41} ж	[40]
R31	$N_4^+ + N \rightarrow 2N_2 + N^+$	1.00×10^{-17}	[37]
R32	$N_2 + N_2 \rightarrow 2N + N_2$	$6.2 \times 10^{-9} \times (T_g)^{-1.6} \times \exp\left(\frac{-113000}{T_g}\right)$	[41]
R33	$N_2 + N_{2,v=1} \rightarrow 2N + N_2$	$6.2 \times 10^{-9} \times (T_g)^{-1.6} \times \exp\left(\frac{-113000}{T_g}\right)$	*
R34	$N_2 + N_{2,v=2} \rightarrow 2N + N_2$	$6.2 \times 10^{-9} \times (T_g)^{-1.6} \times \exp\left(\frac{-113000}{T_g}\right)$	*
R35	$N_2 + N_{2,v=3} \rightarrow 2N + N_2$	$6.2 \times 10^{-9} \times (T_g)^{-1.6} \times \exp\left(\frac{-113000}{T_g}\right)$	*
R36	$N_2 + N_{2,v=4} \rightarrow 2N + N_2$	$6.2 \times 10^{-9} \times (T_g)^{-1.6} \times \exp\left(\frac{-113000}{T_g}\right)$	*
R37	$N_2 + N_{2,v=5} \rightarrow 2N + N_2$	$6.2 \times 10^{-9} \times (T_g)^{-1.6} \times \exp\left(\frac{-113000}{T_g}\right)$	*
R38	$N_2 + N_{2,v=6} \rightarrow 2N + N_2$	$6.2 \times 10^{-9} \times (T_g)^{-1.6} \times \exp\left(\frac{-113000}{T_g}\right)$	*

(Continued.)

Table 2. (Continued.)

	Reaction	Reaction rate coefficient	Reference
R39	$N_2 + N_{2,v=7} \rightarrow 2N + N_2$	$6.2 \times 10^{-9} \times (T_g)^{-1.6} \times \exp\left(\frac{-113000}{T_g}\right)$	*
R40	$N_2 + N_{2,v=8} \rightarrow 2N + N_2$	$6.2 \times 10^{-9} \times (T_g)^{-1.6} \times \exp\left(\frac{-113000}{T_g}\right)$	*
R41	$N_2 + N_{2,v=9} \rightarrow 2N + N_2$	$6.2 \times 10^{-9} \times (T_g)^{-1.6} \times \exp\left(\frac{-113000}{T_g}\right)$	*
R42	$N_2 + N_{2,v=10} \rightarrow 2N + N_2$	$6.2 \times 10^{-9} \times (T_g)^{-1.6} \times \exp\left(\frac{-113000}{T_g}\right)$	*
R43	$N_2 + N_{2,v=11} \rightarrow 2N + N_2$	$6.2 \times 10^{-9} \times (T_g)^{-1.6} \times \exp\left(\frac{-113000}{T_g}\right)$	*
R44	$N_2 + N_{2,v=12} \rightarrow 2N + N_2$	$6.2 \times 10^{-9} \times (T_g)^{-1.6} \times \exp\left(\frac{-113000}{T_g}\right)$	*
R45	$N_2 + N_{2,v=13} \rightarrow 2N + N_2$	$6.2 \times 10^{-9} \times (T_g)^{-1.6} \times \exp\left(\frac{-113000}{T_g}\right)$	*
R46	$N_2 + N_{2,v=14} \rightarrow 2N + N_2$	$6.2 \times 10^{-9} \times (T_g)^{-1.6} \times \exp\left(\frac{-113000}{T_g}\right)$	*
R47	$N_2 + N_{2,v=15} \rightarrow 2N + N_2$	$6.2 \times 10^{-9} \times (T_g)^{-1.6} \times \exp\left(\frac{-113000}{T_g}\right)$	*
R48	$N_2 + N_2\left(A^3\Sigma\right) \rightarrow 2N + N_2$	$6.2 \times 10^{-9} \times (T_g)^{-1.6} \times \exp\left(\frac{-113000}{T_g}\right)$	*
R49	$N_2 + N_{2,v=1} \rightarrow 2N_2$	0.80×10^{-27}	[42]
R50	$N_2 + N_{2,v=2} \rightarrow N_{2,v=1} + N_2$	1.80×10^{-27}	[42]
R51	$N_2 + N_{2,v=3} \rightarrow N_{2,v=2} + N_2$	3.10×10^{-27}	[42]
R52	$N_2 + N_{2,v=4} \rightarrow N_{2,v=3} + N_2$	5.00×10^{-27}	[42]
R53	$N_2 + N_{2,v=5} \rightarrow N_{2,v=4} + N_2$	7.40×10^{-27}	[42]
R54	$N_2 + N_{2,v=6} \rightarrow N_{2,v=5} + N_2$	1.10×10^{-26}	[42]
R55	$N_2 + N_{2,v=7} \rightarrow N_{2,v=6} + N_2$	1.60×10^{-26}	[42]
R56	$N_2 + N_{2,v=8} \rightarrow N_{2,v=7} + N_2$	2.60×10^{-26}	[42]
R57	$N_2 + N_{2,v=9} \rightarrow N_{2,v=8} + N_2$	3.80×10^{-26}	[42]
R58	$N_2 + N_{2,v=10} \rightarrow N_{2,v=9} + N_2$	5.70×10^{-26}	[42]
R59	$N_2 + N_{2,v=11} \rightarrow N_{2,v=10} + N_2$	8.50×10^{-26}	[42]
R60	$N_2 + N_{2,v=12} \rightarrow N_{2,v=11} + N_2$	1.28×10^{-25}	[42]
R61	$N_2 + N_{2,v=13} \rightarrow N_{2,v=12} + N_2$	1.93×10^{-25}	[42]
R62	$N_2 + N_{2,v=14} \rightarrow N_{2,v=13} + N_2$	2.91×10^{-25}	[42]
R63	$N_2 + N_{2,v=15} \rightarrow N_{2,v=14} + N_2$	4.38×10^{-25}	[42]
R64	$N_2 + N_2\left(A^3\Sigma\right) \rightarrow 2N_2$	3.50×10^{-27}	**[40]
R65	$N_{2,v=1} + N_2 \rightarrow N_2 + N_{2,v=1}$	1.00×10^{-20}	[43]
R66	$N_{2,v=1} + N_{2,v=1} \rightarrow N_2 + N_{2,v=2}$	2.00×10^{-20}	[43]
R67	$N_{2,v=1} + N_{2,v=2} \rightarrow N_2 + N_{2,v=3}$	3.00×10^{-20}	[43]
R68	$N_{2,v=1} + N_{2,v=3} \rightarrow N_2 + N_{2,v=4}$	3.50×10^{-20}	[43]
R69	$N_{2,v=1} + N_{2,v=4} \rightarrow N_2 + N_{2,v=5}$	3.65×10^{-20}	[43]
R70	$N_{2,v=1} + N_{2,v=5} \rightarrow N_2 + N_{2,v=6}$	3.60×10^{-20}	[43]
R71	$N_{2,v=1} + N_{2,v=6} \rightarrow N_2 + N_{2,v=7}$	3.25×10^{-20}	[43]
R72	$N_{2,v=1} + N_{2,v=7} \rightarrow N_2 + N_{2,v=8}$	3.00×10^{-20}	[43]
R73	$N_{2,v=1} + N_{2,v=8} \rightarrow N_2 + N_{2,v=9}$	2.50×10^{-20}	[43]

$f(\varepsilon)$: reaction rate obtained from EEDF with associated cross-section data. All rate coefficients are in units m^3s^{-1} except for three-body reactions denoted by '$\divideontimes$' in which cases, rate coefficients are in units m^6s^{-1}

Key: *based on similarity to R32. **: based on similarity to reactions in [40].

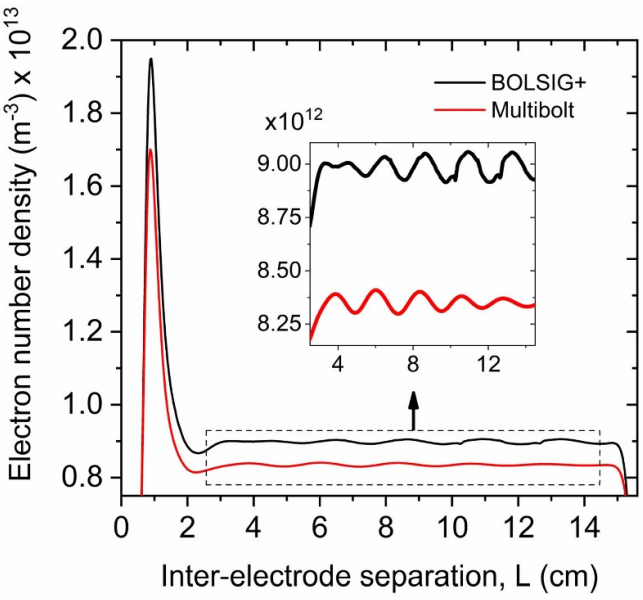

Figure 2. Comparison of electron number density predicted from a BOLSIG+ and MultiBolt as inset ($P = 0.7$ Torr, $L = 15.5$ cm, $V_d \sim 380$ V, $J_d \sim 0.018$ mA cm^{-2}).

into account the effects of non-Maxwellian EDF on the fluid model results.

Figure 2 compares the predicted axial distribution of the electron number density (n_e), between the BOLSIG+ and MultiBolt data. For both the datasets, the simulations are performed so that almost identical discharge voltage and current are attained. Despite the near-identical discharge voltage and current, it is evident that in the case of the two term-approximation, the higher intensity striations lie closer to the anode and vice versa in the case of the MultiBolt. Distinct differences between the predicted spatial profiles of the striations are present between the two data sets. The differences exist in the striation number and the amplitude of the undulations.

Ionization rate and transport coefficients calculated from the two-term and multi-term BE equation are presented in figure 3. As shown, the ionization rate as calculated via two-term and multi-term solutions to the BE are nearly identical. A similar agreement is observed for the electron mobility up to ∼600 Td, beyond which the two-term and multi-term results begin to deviate. At 1000 Td, the differences in mobility are ∼3% and increase to ∼9% at 2000 Td. The diffusion coefficients demonstrate even higher sensitivity with ∼14% variations in the transverse diffusion coefficient at 500 Td and a similar level at 2000 Td. Even more significant deviation is observed for the longitudinal diffusion coefficient, with ∼18% difference between the two models at 500 Td and up to ∼90% at 2000 Td.

Figure 4 compares the excitation rates calculated from two-term and multi-term solutions. These excitation rates represent the general behavior observed with excitation to low energy (sub-eV), moderate energy (few eV), and high energy (10 + eV) excited states. Comparing excitations to the lowest vibrational levels demonstrates a 5%–10% disparity at ∼120 Td. However, the models are in a notable better agreement at higher reduced electric fields. Similar observations are made for moderate energy excitations. The models agree well below ∼400 Td, deviate by ∼2% in the range 500–1500 Td, then again at higher values of Td. Finally, the models agree well for the highest energy excitation, up to 1000 Td, where they begin to deviate from one another. At 2000 Td, the disagreement between the models is ∼3.5%. Overall, unlike the transport parameters, the disparity between the calculated excitation rates is relatively small, indicating the EDF's strongest anisotropy for low-energy electrons.

These results re-emphasize the long-known shortcoming of the two-term approximation for molecular nitrogen [49]. Notably, the transport coefficients could be of error about 5% in the range of 100 Td, which is the most relevant range of reduced electric field for this study. The electron diffusion coefficient strongly influences the structure of stratified plasma. Thus, one would expect that the differences between the two-term and multi-term calculated coefficients would lead to cascading differences in predicted plasma structure when these coefficients are utilized in a fluid model.

Similar observations may be made for the excitation rates. Molecular nitrogen has a large number of vibrational excitations with large cross-sections, which dominate the electron energy dissipation in the low energy range. An error in calculating these excitation rates affects the overall energy balance of electrons in the plasma. The error in the excitation rates of the lowest vibrational levels of N_2 was on the order of 5%–10% in the range of reduced electric field of relevance to this study (∼100 Td). Thus again, one may expect that accurate excitation rates improve the accuracy of the fluid plasma model.

4. Experimental setup

We measured the voltage-current characteristics and recorded the visual appearance of the striations. A schematic of the experimental setup is shown in figure 5. A dc power supply (Glassman 0 – 20 kV, 300 W) is connected in series to a ballast resistor (100 kΩ), the low-pressure plasma cell, and a shunt resistor (10 kΩ) to measure the discharge current. A high voltage probe (North star PVM-4) and an oscilloscope probe (Tektronix M12) are used to measure the voltage drops across the discharge and the shunt, respectively; both the probes are connected to a mixed-signal oscilloscope (Keysight MSO7054B). The discharge is enclosed in a cylindrical plasma cell consisting of a 16.0 cm (maximum operable length of 15.5 cm) long and 3.71 cm outer diameter cylindrical tube of borosilicate glass with two stainless steel disk electrodes on the opposite ends.

The electrodes have a diameter of 3.65 cm. The electrode arrangements are such that before conducting the experiments,

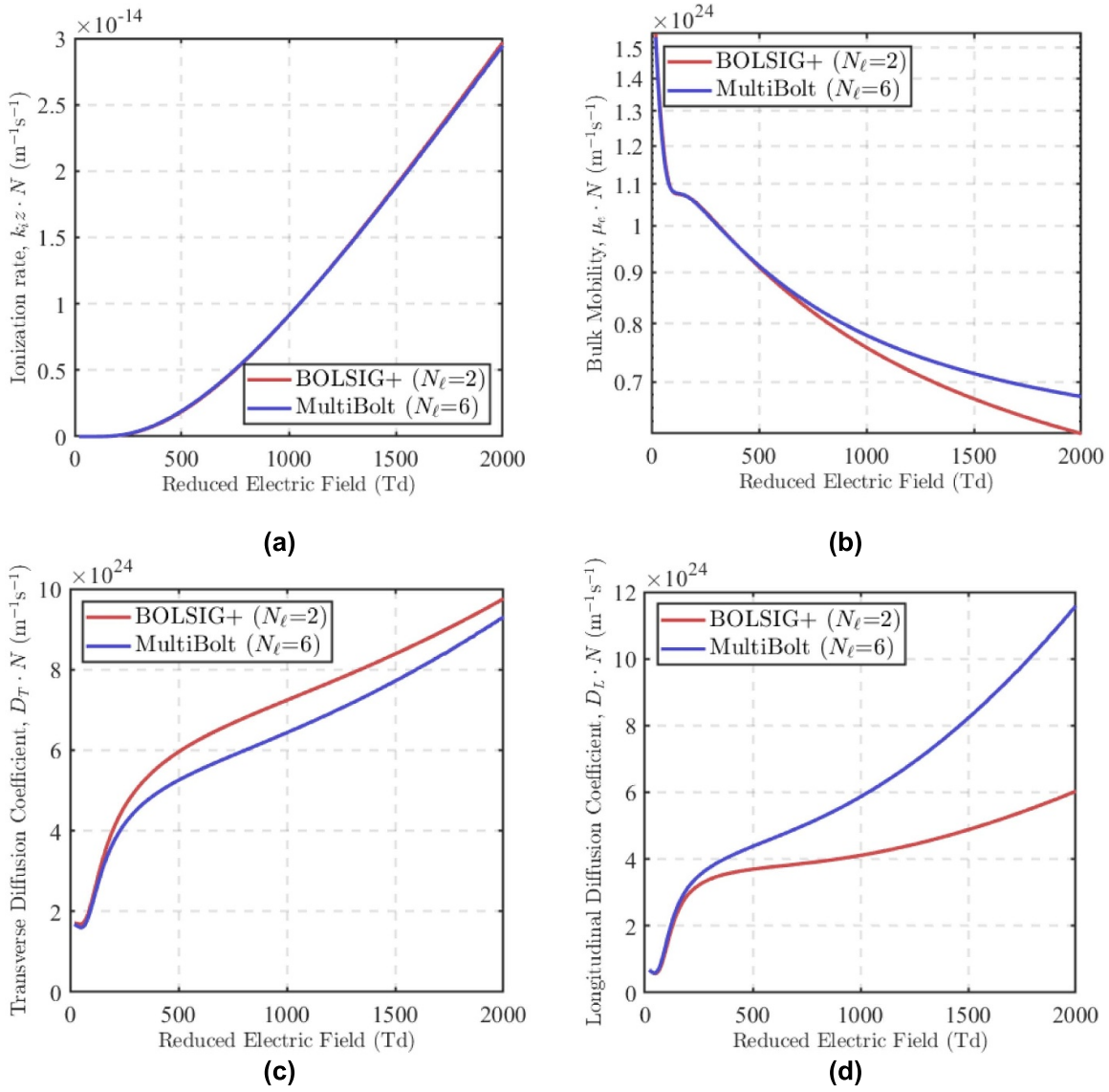

Figure 3. Comparison of (a) ionization rate (b) bulk electron mobility (c) bulk transverse diffusion coefficient (d) bulk longitudinal diffusion coefficient, as a function of reduced electric field calculated from two-term and multi-term solutions to the Boltzmann equation in N_2.

the inter-electrode distance can be varied. The discharge cell is connected to a vacuuming system through ultra-torr conflate flanges. Additional fittings include a pressure gauge, a valve connecting the vacuum pump and an inlet valve for supplying fresh high-purity nitrogen gas. The pressure is measured with a Teledyne Hastings 760s gauge. The vacuum is attained and maintained with an Agilent IDP-15 dry scroll vacuum pump. The outer periphery of each stainless-steel electrode is wrapped with polyamide tape (Kapton) on the sides to prevent the discharge from diffusing in between the glass tube and electrode gap at low pressures. A Nikon D7000 digital camera is used to image the light emission over a range of discharge current conditions. Each image was captured over an exposure time of 3 s with a NIKKOR 18–55 mm f/3.5–5.6 G lens with focal length, aperture, and ISO set to 32 mm, f/4.5 and ISO-200, respectively.

5. Results and discussion

The simulations are conducted for 0.7 Torr operating pressure (P) with an inter-electrode separation distance (L) of 15.5 cm (i.e. $PL = 10.85$ Torr cm) and electrode diameter of 1.1 cm. The discharge current/current density is varied to determine its effect on the striation structure. Figure 6 shows the spatial distribution of the electron number density (n_e), (figure 6(a)), the electric potential, electric field and the electron temperature (T_e) (figure 6(b)) for the base case. These spatial distributions represent a quasi-steady-state solution that the system reaches in 0.25 ms. At this stage, no noticeable transient variation in discharge current (I_d) and discharge voltage (V_d) is observed, as seen in the figure 6(b) inset. The n_e distribution shows a steady undulated profile representing a striated structure. The undulations occur outside the cathode sheath, in the

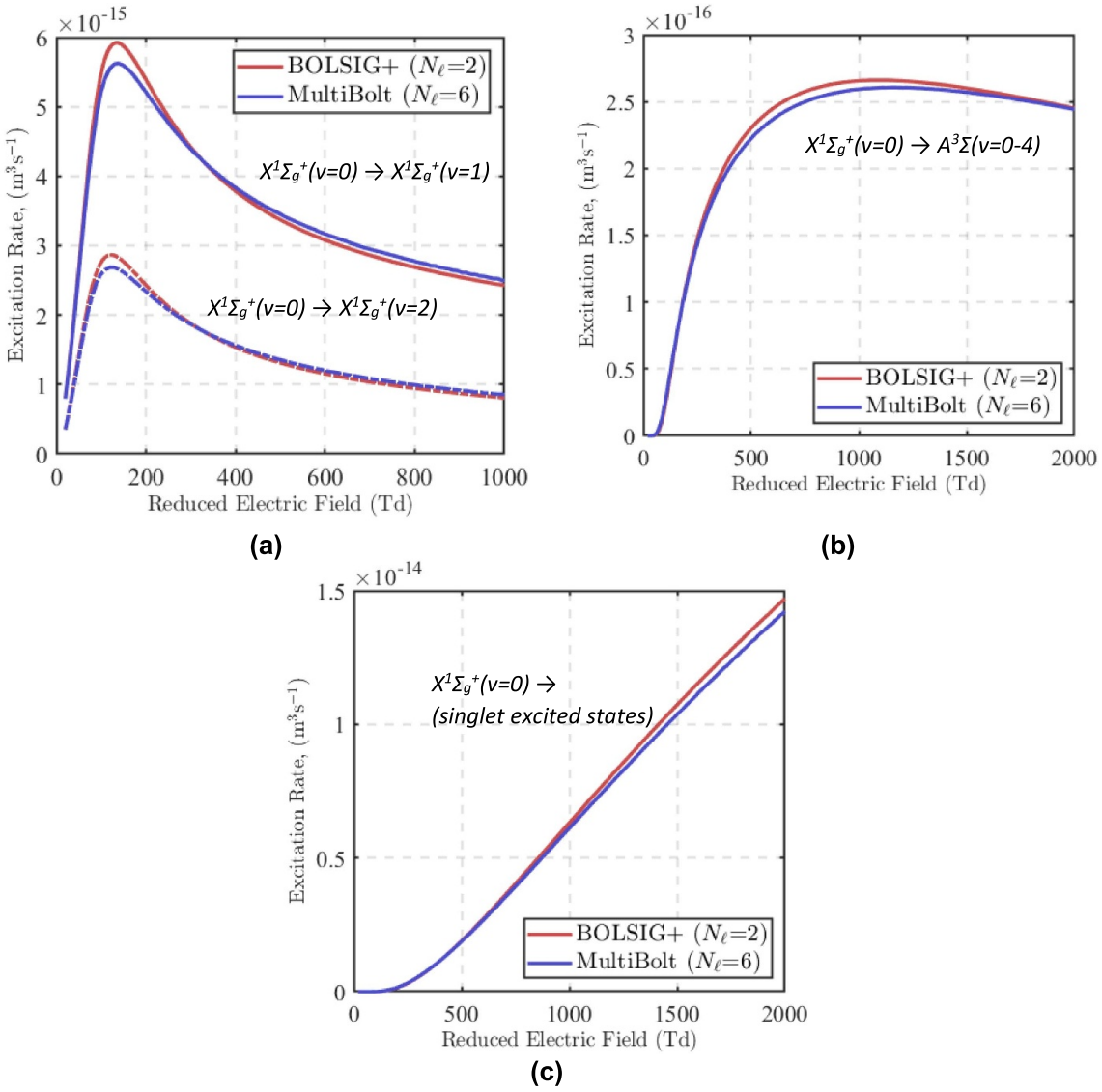

Figure 4. Comparison of (a) excitation rates to the first two vibrational levels of molecular nitrogen (threshold energies of 0.29 eV and 0.5742 eV, respectively), (b) excitation rate to the first five vibrational levels of the $A^3\Sigma$ excited state (threshold energy of 6.73 eV), and (c) summed rate of excitation for all singlet states of N_2 (threshold energy of 14.2 eV), as a function of reduced electric field calculated from two-term and multi-term solutions to the Boltzmann equation in N_2.

positive column region where the potential increases linearly (see figure 6(b)). Five strata are formed in between ∼2.2 and 13.8 cm, with the electron density modulations between ∼8.28 and 8.44 × 10^{12} m^{-3}.

The modulation of the electron number density and striation length decrease towards the anode. The first two striations have maximums n_e of 8.39 × 10^{12} m^{-3} and 8.41 × 10^{12} m^{-3} and width of ∼1.3 cm, based on the full-width half maximum. Further, towards the anode, the density modulation decreases to 8.4 × 10^{12} m^{-3}, 8.38 × 10^{12} m^{-3} and 8.37 × 10^{12} m^{-3} and the width decreases to ∼1.23 cm, 1.22 cm and 1.20 cm, respectively. Similar experimental observations have been reported by Lisovskiy *et al* [7], in which the width of the striations decreases progressively towards the anode. The n_e peaks coincide with the dip in T_e (figure 6(b)) — the electron energy generally being depleted due to the ionization processes. Analysis shows that the net source of electrons and the ambipolar diffusion losses balance over striation length.

The electric potential profile clearly shows the cathode sheath and a positive column plasma with a constant electric field (figure 6(b)). A closer look shows noticeable oscillations of the electric field in plasma, with four fully developed modulations and one partially developed close to the anode; the amplitude of the modulations for the first two strata are ∼ 30 Vm^{-1}. This amplitude subsequently decreases to ∼18 and ∼11 Vm^{-1} in the third and the fourth strata. The electron temperature T_e follows the electric field distribution and fluctuates between ∼1.60 and 1.66 eV in the striated plasma.

Figure 7 illustrates the spatial profiles of the charged species. The electrons and total ions densities deviate in the cathode and anode sheaths but are almost the same in the plasma region (insets figure 7(a)). The presence of the small

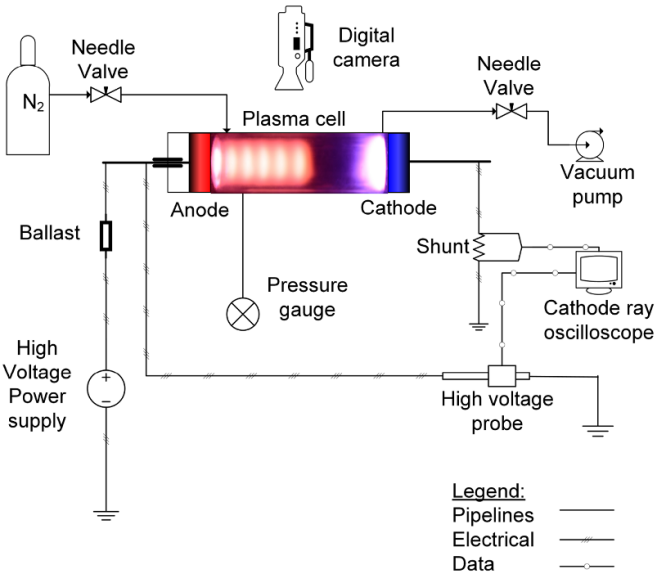

Figure 5. Schematic of the experimental setup.

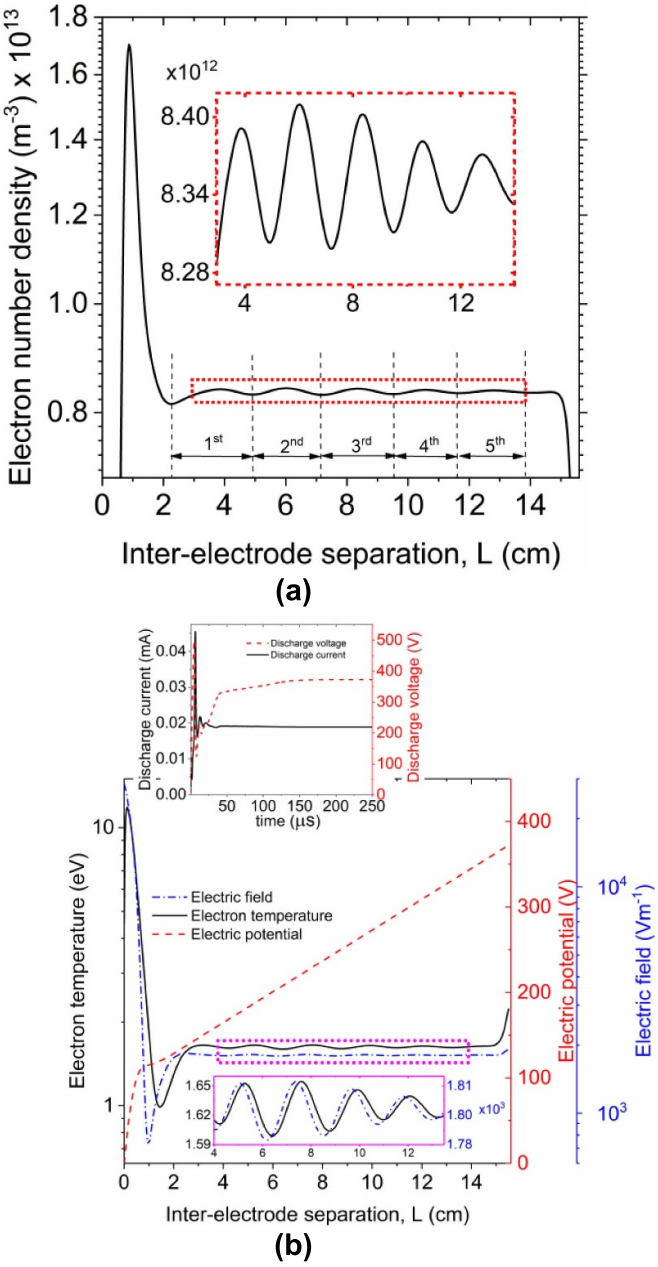

Figure 6. Quasi-steady spatial distribution of (a) electron number density and (b) electric potential, electric field and electron temperature along the axial distance.($V_d = 370$ V, $J_d = 0.018$ mA cm^{-2}).

space charge in plasma is consistent with the oscillation in the electric field. The simulations identify N_2^+ as the dominant ion in the cathode sheath (figure 7(b)) and the plasma region.

The spatial distributions of different ions in the striated plasma are distinctively different (figure 7(b)). The density of N_2^+ ion is significantly higher, and its oscillations are of higher amplitude compared to those of N^+ and N_4^+. In addition to the main channel of electron impact ionization, the N^+ and N_4^+ ions are formed by the charge exchange processes (R30: $N_2^+ + 2N_2 = N_2 + N_4^+$ and R31: $N_4^+ + N = 2N_2 + N^+$). These processes are not sensitive to the electric field strength. However, since N_2 and N_2^+ are more abundant in the system than N_4^+ and N, the N_4^+ density is higher than that of N^+.

Figure 8 depicts the spatial distributions of the vibrationally excited and the electronically excited $N_2(A^3\Sigma)$ species. Even though the spatial profiles of the vibrational excitation reaction rates (R2-R17) follow the n_e profile in the positive column (not shown here), smaller oscillations are seen for each vibrationally excited molecule. The reason is that the vibrationally excited species are partially formed through the vibrational-relaxation (R49-R63) and the vibrational-vibrational (R65-R73) interactions, which do not depend on either T_e or n_e. The vibrationally excited species with lower excitation thresholds have the highest density. The $N_2(A^3\Sigma)$ distribution exhibits a similar profile as that of the vibrationally excited states. The predictions further show that despite requiring a higher threshold excitation energy (i.e. ∼6.73 eV), the $N_2(A^3\Sigma)$ density is higher than the $N_{2,v=8}$ state, which has a much lower excitation energy (∼2.21 eV). The electronically excited $N_2(A^3\Sigma)$ state is not solely formed through direct electron impact, but also through a stepwise process involving $N_{2,v=1}$ (R19: $e + N_{2,v=1} = e + N_2(A^3\Sigma)$), which is present in higher abundance than other vibrational species owing to its lowest excitation potential. Outside of the cathode fall, where the electron kinetic energy is lower, the low-energy chemical processes dominate.

Figures 9–11 illustrate the axial distribution of the reaction rates for N_2^+, N^+ and N_4^+ respectively. The electron/ion sources are shown by solid lines, and the dashed lines show the sinks. The electron impact ionization reactions of N_2, $N2_{,v}=1$, and N (i.e. R23, R24 and R25), which have the highest ionization potential, are the most effective in the cathode sheath region (figure 9), where the electron kinetic energy is higher. Even outside the cathode fall, N_2^+ is predominately formed

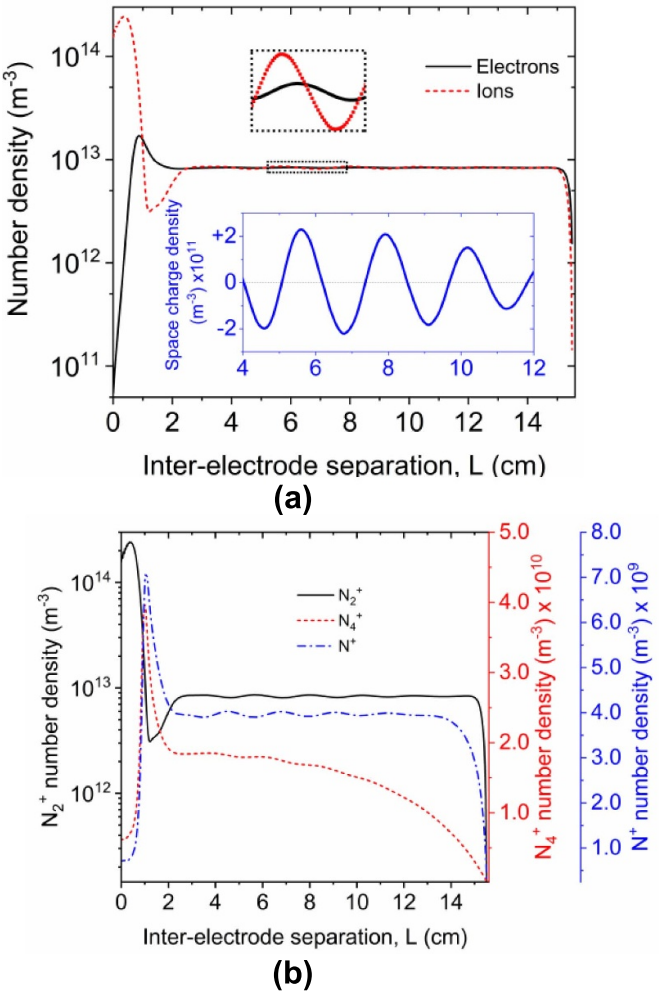

Figure 7. Quasi-steady spatial distribution of (a) electron, total ions and (b) three different ions. Zoomed view of the space charge density in the striated positive column region is provided as an inset. ($V_d = 370$ V, $J_d = 0.018$ mA cm^{-2}).

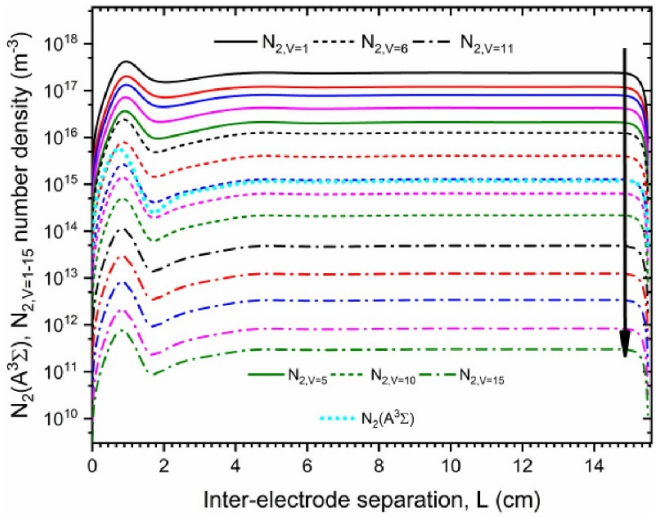

Figure 8. Spatial distribution of the different excited species along the axial distance ($V_d = 370$ V, $J_d = 0.018$ mA cm^{-2}).

by electron impact, R23: e + N_2 → 2e + N_2^+ (figure 9(b)). All three of these reaction rates are modulated in the striated plasma but have much lower rates than in the sheaths. The ionization from N2,$_v$=1 (R24) in the striated plasma is three orders of magnitude lower than R23 despite having a slightly lower energy threshold. Even though $N_{2,v=1}$ requires lower energy than ground state N_2, the number density of ground state N_2 is significantly higher. Thus, the collision frequency of high-energy electrons with the ground state N_2 will always be higher than that with N2,$_v$=1. For most stratified plasma, the dissociative recombination (R29: e + N_2^+ → 2N) acts as a major consumption path and exceeds both the three-body recombination rates (R26: 2e + N_2^+ → e + N_2 and R27: 2e + N^+ → e + N). The model considered here incorporates the stepwise ionization of only N2,$_v$=1, the first vibrationally excited species of N_2. Data on stepwise ionization rate coefficients and/or collision cross-sections are very scarce in the literature. Cacciatore *et al* considers the reaction cross-section data for step-ionization of N2,$_v$=5 and $N_{2,v=10}$ species but only for a limited electron energy range that could not be reasonably extrapolated for the present study [54]. Due to the limited availability of cross-section and reaction rate coefficients for the required electron energy range and different excited states, stepwise ionizations from all the other vibrational states were not included in the present study.

The formation of N^+ from heavy particle interaction is compared with the three-body recombination and presented in figure 10. The N^+ formation in plasma occurs through charge transfer (R31: N_4^+ + N → 2N_2 + N^+). The rate of this reaction is larger than that of the three-body recombination rate of N^+ (R27: 2e + N^+ → e + N) for most of the positive column and follows the profile of N_4^+. The N_4^+ ions are formed predominantly by reaction between N_2 and N_2^+ (R30: N_2^+ + 2N_2 → N_2 + N_4^+, see figure 11); the electron impact dissociative recombination reaction (R28: e + N_4^+ → 2N + N_2) remains as the most active consumption channel. Further comparisons among figures 9–11 indicate that for both N_2^+ and N^+, the recombination rates exceed the formation rates in the plasma. The dominance of recombination over production rate has been identified by Kawamura *et al* [9] as a source of instability and plasma stratification. However, for N_4^+ ions formed through the charge transfer, the formation rate (R30) exceeds the recombination rates (R28 and R31).

Simulations were conducted by eliminating the vibrational excitation reactions ($N_{2,v=1-15}$) and compared with the base case results (figure 12) for the same discharge voltage and current. Without vibrational excitation reactions, the striations did not form. Omitting only the $N_2(A^3\Sigma)$ excitation, N-elastic and N-ionization reactions from the reaction scheme did not have any noticeable effect on the striations (not shown here). Previous studies [23, 27] have demonstrated that excluding the loss term due to ambipolar diffusion to the wall fails to produce the positive column. In our case, both the ambipolar diffusion to the wall and the vibrational excitation reactions play key roles in forming the standing striation in molecular nitrogen gas. An interesting observation in the profile of T_e

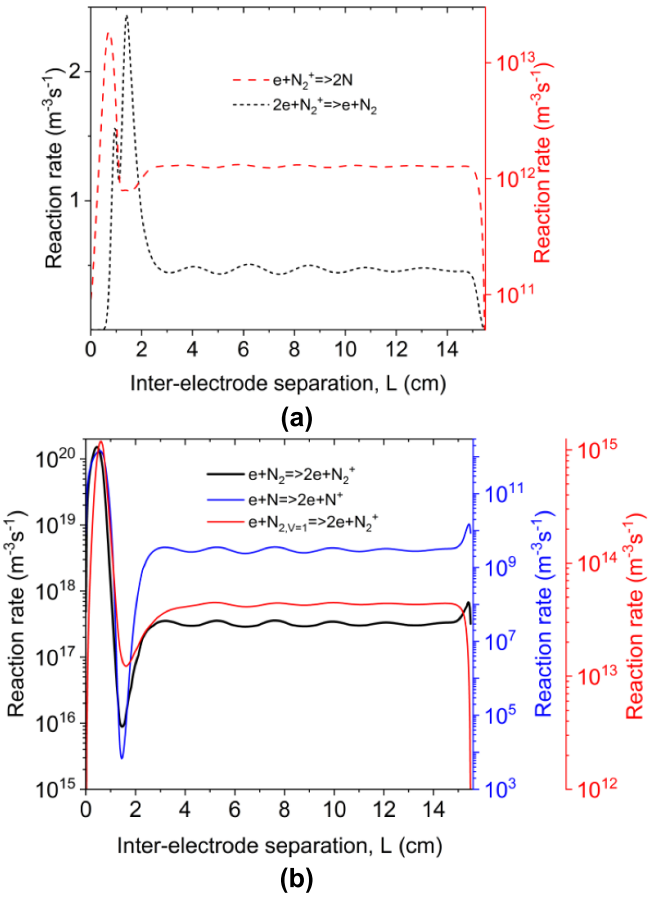

Figure 9. Spatial distribution of (a) recombination and (b) ionization reaction rates of N_2^+ ions along the axial distance ($V_d = 370$ V, $J_d = 0.018$ mA cm^{-2}).

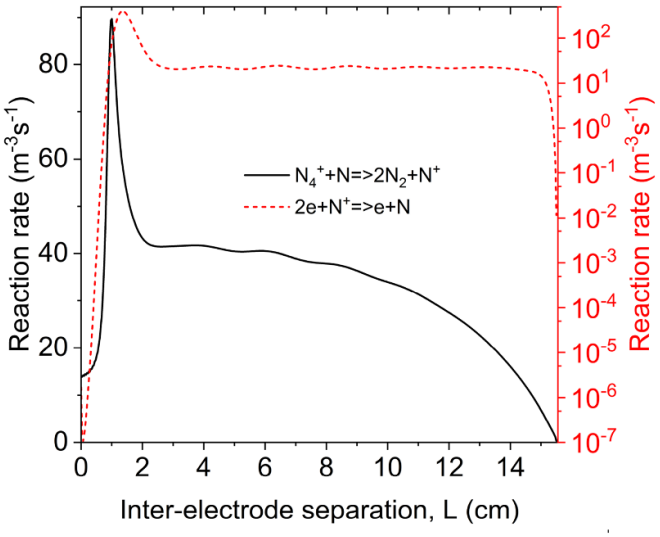

Figure 10. Distribution of the ionization and recombination reaction rates of N^+ ions along the axial distance ($V_d = 370$ V, $J_d = 0.018$ mA cm^{-2}).

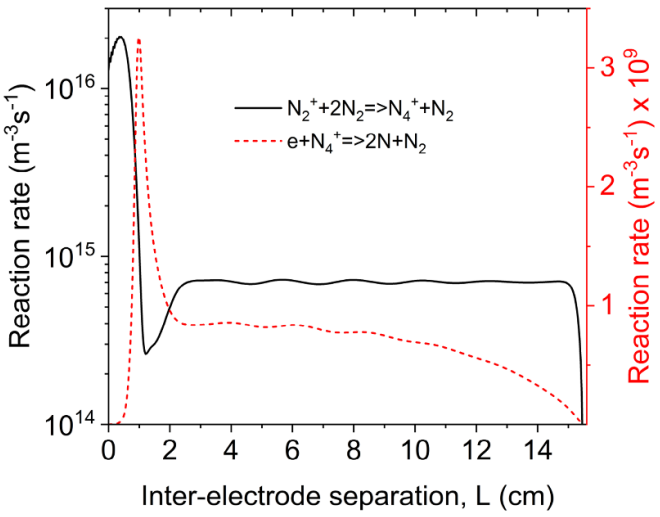

Figure 11. Distribution of the ionization and recombination reaction rates of N_4^+ ions along the axial distance ($V_d = 370$ V, $J_d = 0.018$ mA cm^{-2}).

(figure 12(b)) is that without the vibrational excitation reactions, T_e remains around 1.63 eV in the positive column. This value of ∼1.63 eV is also the mean value of the electron temperature T_e in the presence of striations with the vibrational reactions included in the model. One would expect that the value of T_e would increase in the absence of the vibrational excitations channel. However, that is not the case. As always happens in non-equilibrium plasmas, the electron temperature is adjusted to satisfy the balance of the production and losses.

The spatial distribution of n_e for a range of discharge current densities is presented in figure 13(a). The discharge operates in the 'abnormal' glow mode (see figure 17(b)). As a result, the current density increases with the discharge voltage. The predictions clearly show that as the current density increases, the number of striations decreases. The striations tend to get shorter, as observed in the experiments (figure 17(a)). At higher current densities beyond 0.080 mA cm^{-2}, the striations are absent, and the positive column plasma is axially uniform (not shown here). As the discharge current increases, the amplitude of the T_e modulation decreases, and the T_e value tends to approach ∼1.63 eV (figure 13(b)).

Figure 14 compares the total formation and consumption rates for the ions and electrons mapped across the entire electron temperature range of discharges at two values of current densities. These rates were obtained by summing all the independent sources and sinks for the charged species, including the radial losses from ambipolar diffusion. For both cases, the electron and ion formation rates are almost identical and respective profiles overlap. In figure 14(a), unlike the continuous increasing ion consumption rate, the electron consumption rate increases only up to ∼3.3 eV and then tends to decrease much rapidly. The electron and ions formation and consumption rates start to become comparable to each other in between ∼1.3 and 2 eV, especially at T_e ∼ 1.63 eV they become almost equal to each other. A closer look (figure 14(a) inset) at the rates shows a distinct hysteresis between the ion and electron consumption rates at T_e ∼ 1.60–1.66 eV, which is the T_e modulation amplitude in the striations. Figure 14(b) shows

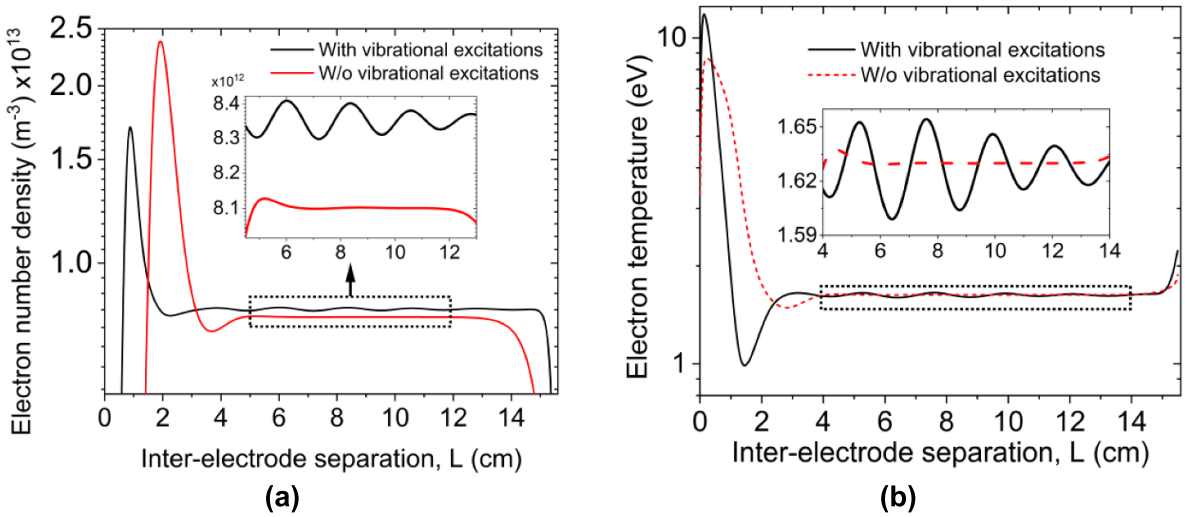

Figure 12. Impact of vibrational excitation reactions ($e + N_2 \rightarrow e + N_{2,\,v=1-15}$) on the (a) electron number density, and (b) electron temperature distribution along the axial distance.

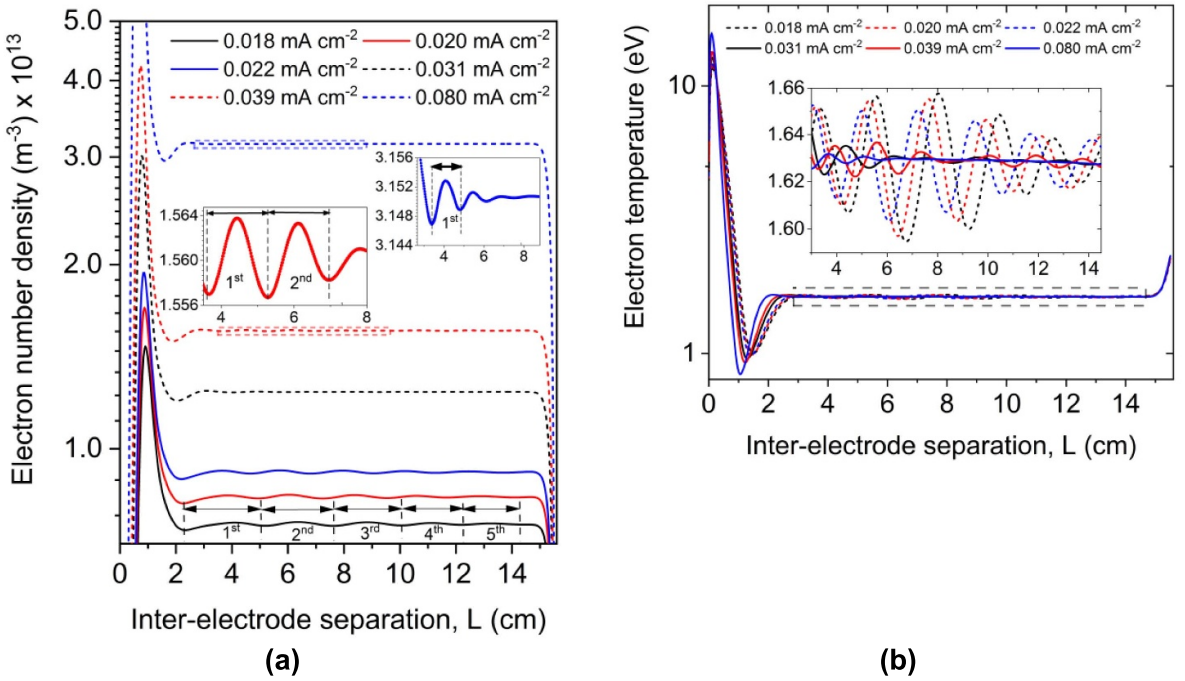

Figure 13. Predicted spatial distribution of electron (a) number density and (b) temperature distribution for different discharge current densities.

that there is a greater degree of overlap between the ion and electron consumption rates for higher current density, and the hysteresis behavior is nearly absent. Comparison of the consumption rates for ions and electrons suggests that significant differences between the ion and electron consumption rates and possible hysteresis characteristics of the consumption rates at the lower range of electron temperature (1.0–2.0 eV) can trigger instability in the system that can result in plasma stratification.

The impact of the vibrational excitation reactions on the electron heating ($\vec{j}_e.\vec{E} - \Delta e_{\text{loss from vibration excitation}}$) is illustrated in figure 15(a), which shows the joule heating and electron number density for two modulations (x = 7.4 – 11.4 cm) for two current densities. It is evident that the joule heating profile is entirely out of phase with n_e. At a lower current density, both the n_e and the power source oscillate with higher amplitude. At 0.022 mA cm^{-2}, the power oscillates between ∼4 and 9 Wm^{-3}, and the reduced electric field oscillates between 78 and 82 Td. Most of the power absorbed by electrons is lost to vibrational and electronic excitation [55]. As the current density increases, the modulation amplitude of the energy source diminishes to 0.2 Wm^{-3}, which is equivalent to a reduction in the oscillating amplitude by ∼96%. This implies that the vibrational excitation reactions do not significantly perturb the

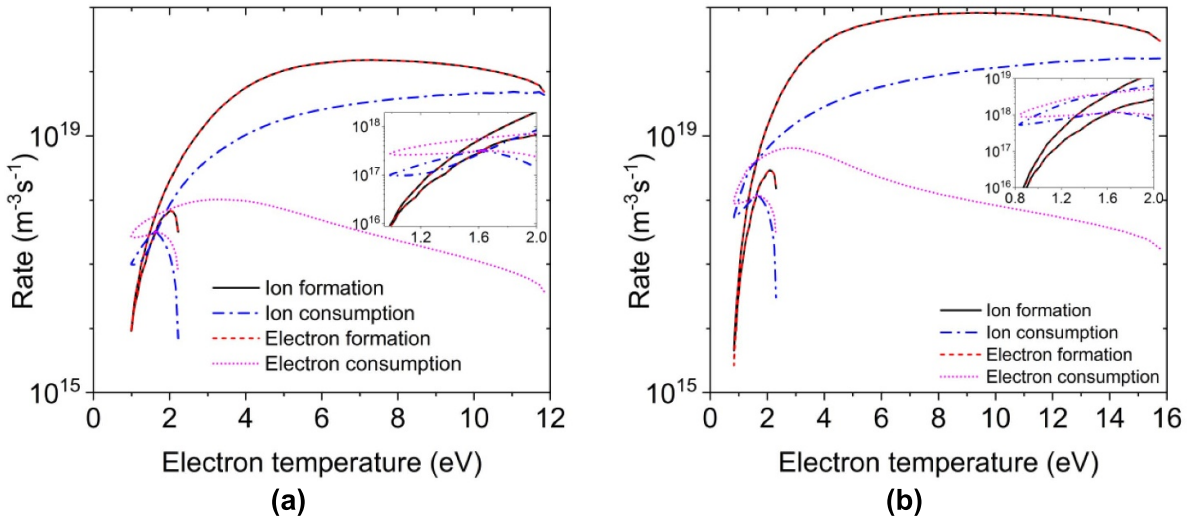

Figure 14. Ion and electron formation and consumption rate as a function of electron temperature during standing striations for operating discharge parameters of (a) ($V_d = 370$ V, $J_d = 0.018$ mA cm^{-2}) (b) ($V_d = 388$ V, $J_d = 0.081$ mA cm^{-2}).

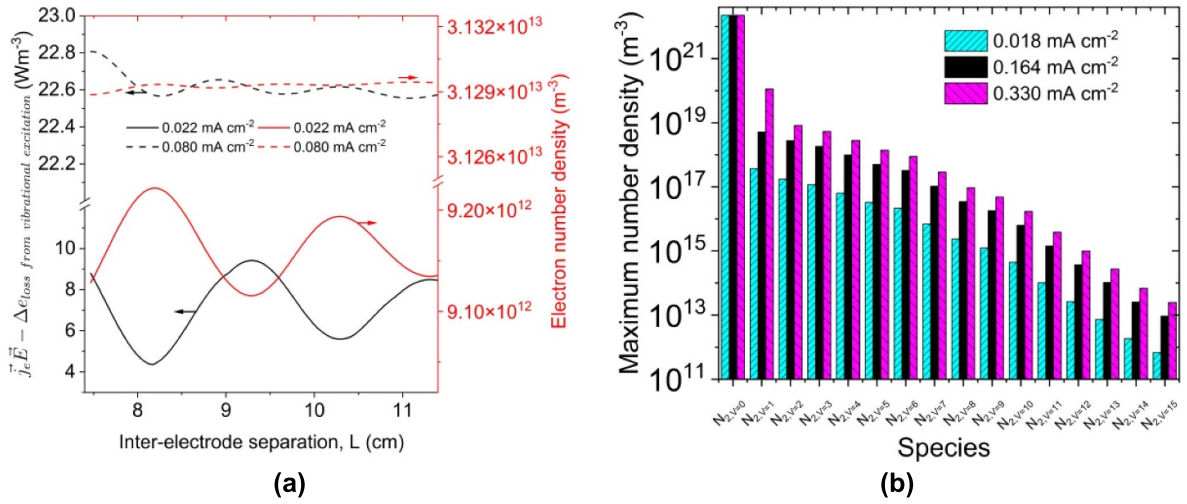

Figure 15. (a) Spatial variation of $\vec{j}_e.\vec{E} - \Delta e_{\text{loss from vibration excitation}}$ and electron number density in the striated region (b) distribution of vibrationally excited species for different current densities.

Joule heating term at higher current and voltage. The distributions of the vibrationally excited species for three different current densities are presented in figure 15(b). The vibrational species distribution tends to conform towards a Maxwellian-like profile at higher currents.

Figure 16 shows the spatial distributions of the electric field, electron temperature, n_e, n_{ion}, $\frac{dn_e}{dt}$ and $\frac{dn_{ion}}{dt}$, and the phase differences between these in the striated region. The electric field leads the electron temperature by $\sim 0.211\pi$. The phase shift between T_e and n_{ion} is $\sim 0.206\pi$ with n_{ion} lagging T_e (figure 16(a)). However, the electron temperature lags $\frac{dn_{ion}}{dt}$ by $\sim 0.083\pi$. On the other hand, both n_e and $\frac{dn_e}{dt}$ lag T_e by $\sim 0.656\pi$ and 0.156π, respectively (figure 16(b)). The maximum of electron energy perturbation is shifted towards the cathode when compared to both n_e and n_{ion}. The maximum electron energy contributes to the highest ionization rate, and the newly produced electrons tend to move the maximum electron number density towards the anode. However, the electron energy transport along the density gradient (i.e. Dufour effect) tends to shift the peak of the electron energy towards the cathode. Hence, the ionization and the Dufour effect act against each other, and a balance between these two effects results in standing striations.

The variation of the density-gradient-dependent diffusivity, $\chi_\varepsilon = D_\varepsilon - \left(\frac{\mu_\varepsilon}{\mu_e}\right) D_e$ [19] is shown in figure 17 as a function of electron temperature. The distribution indicates that χ_ε is predominantly negative except for a narrow range at low T_e ($\sim$1.5 – 2.25 eV) and at high T_e (i.e. $T_e > 22.5$ eV). Desangles *et al* [19] showed that a sufficiently large negative value of χ_ε can generate instability in the system, which is consistent with our predictions. However, the narrow T_e range of $\sim$1.5 – 2.25 eV across which χ_ε changes sign, coincides with

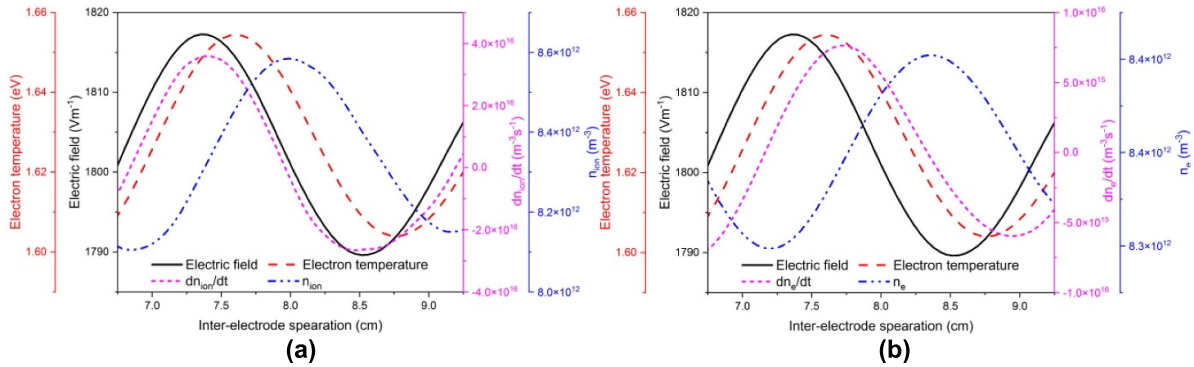

Figure 16. Spatial evolution of (a) n_{ion}, $\frac{dn_i}{dt}$, electric field, electron temperature and (b) n_e, $\frac{dn_e}{dt}$, electric field, electron temperature ($V_d = 370$ V, $J_d = 0.018$ mA cm^{-2}).

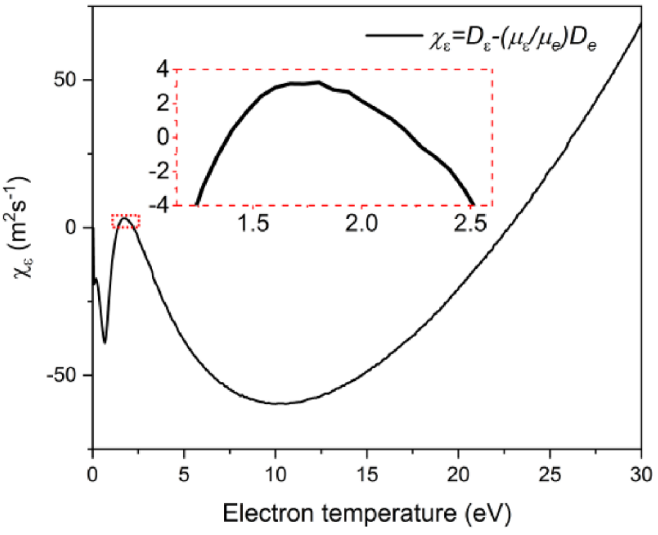

Figure 17. Variation of density gradient dependent diffusivity χ_ε (Dufor effect) as a function of electron temperature.

the T_e modulation range that we have obtained in the striated positive column.

The experiments are conducted at $P = 0.7$ Torr and an inter-electrode separation of $L = 15.5$ cm. The current–voltage-current characteristics have been measured together with visual observation of the discharge (figure 18). The discharge visualization shows that as the current increases, the number of striations tends to decrease but the striation thickness increases. Furthermore, the cathode region (Faraday dark space) expands, and the positive column with striations is shifted towards the anode (figure 18(a)). Figure 18(b) compares the predicted and measured striation lengths directed from the cathode towards the anode. The comparison is conducted for the base case for which, at least five standing striations are visible. This represents the lowest current density conditions. It is seen that in both experiments and simulations, the striation lengths decrease from the cathode to the anode, showing qualitative agreement. It is expected that the addition of nonlocal ionization by fast electrons in future work will result in better quantitative agreement with the experiments for the striation length, not only drastically improve the predictions of the Faraday dark space.

The spatial profiles of n_e from our simulations (figure 13(a)) qualitatively capture the dependence of the striation number on the discharge current. The peak n_e increases as a function of discharge current and can be related to the observed increase in emission intensity of the cathode glow in the experiments. The full width half maximum (FHWM) of the predicted n_e in the negative glow increases with the discharge current. However, the length of the Faraday dark space is much shorter compared to the visual observations. Even though the model can reproduce qualitative trends of the striation behavior (i.e. number of striations), the most considerable discrepancies with the experimental observations are for the Faraday dark space. The predicted striation width decreases with increasing the current density. Additionally, as the discharge current density increases, the predicted strata tend to constrict axially towards the cathode rather than towards the anode location. In our simulations, the width of the cathode region does not change significantly with increasing the discharge current. The cathode-directed constriction of the strata could be a result of that. The experimentally observed increase of the Faraday dark space is due to nonlocal ionization by the fast electrons from the cathode sheath [56], which is currently not captured by the model.

The measured and predicted voltage–current (figure 18(c)) characteristics clearly show the discharge operating in the 'abnormal' glow mode. However, a substantial discrepancy exists between the absolute values obtained in simulations and the experiments. These discrepancies are attributed to the deficiencies of the fluid model, which can not capture nonlocal effects in the cathode region. The experimental observations of plasma emission in both the cathode region and striated positive column show radial gradients, which a one-dimensional model can not accurately capture. A two-dimensional model is currently under development.

Following the work of Urbankova and Rohlena [20] we performed a linear stability analysis of the striation behavior in low-pressure dc nitrogen plasmas. From the linear analysis, the dispersion (ω_r) and the application (ω_i) have the following expressions:

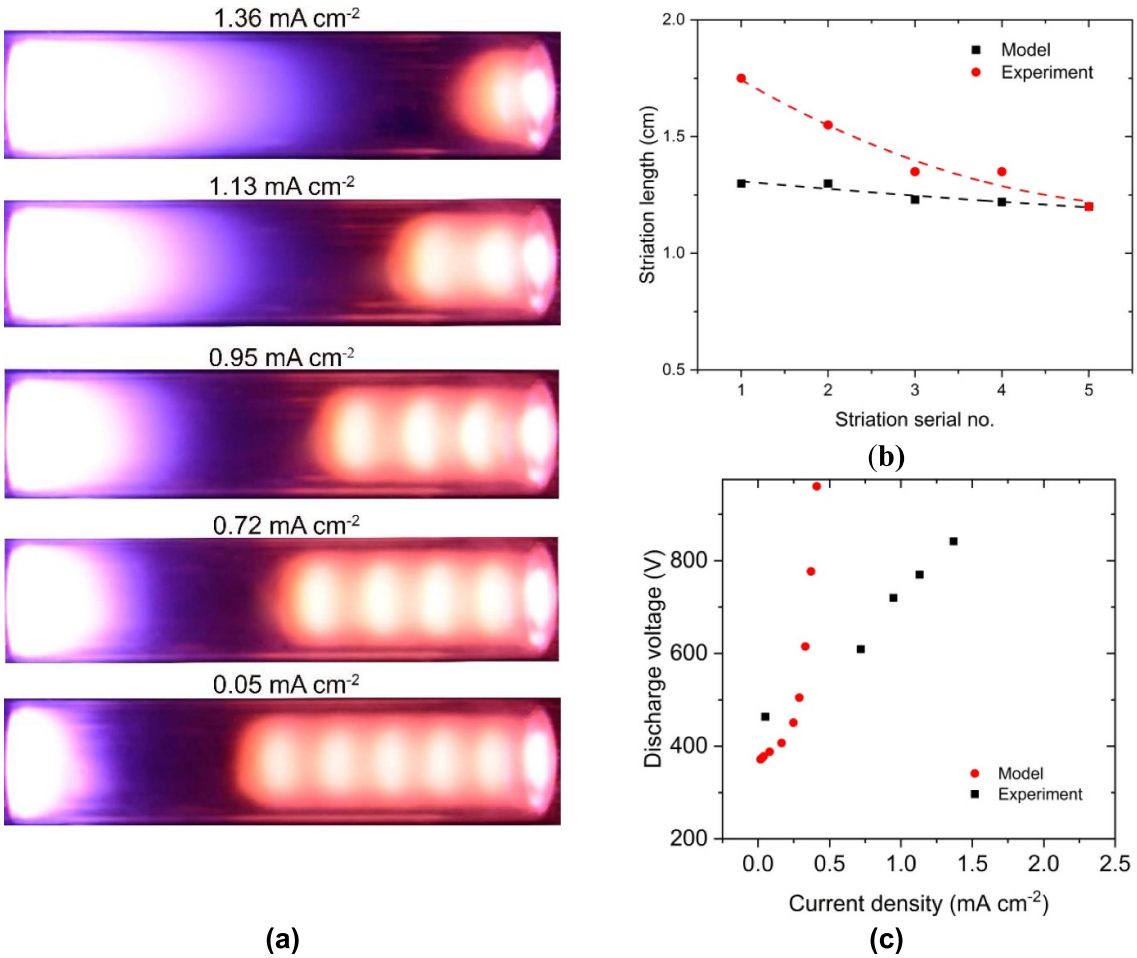

Figure 18. (a) Images of the plasma structure for different discharge densities, (b) comparison of measured and predicted striation lengths, (c) comparison of measured and predicted voltage-current characteristics.

$$
\begin{aligned}
\frac{\omega_r}{D_a} &= \left[\left(\frac{2.4}{R_{\text{tube}}}\right)^2\left(S_{\text{ioniz}|\varepsilon}-1\right)-\eta_e k^2\right]\frac{k\varepsilon}{E_x}\frac{\Upsilon_1}{\Upsilon_2}+\frac{\mu_{e|\varepsilon}E_x}{\varepsilon}k\frac{\Upsilon_3}{\Upsilon_2}\\
\frac{\omega_i}{D_a} &= -k^2\frac{D_e}{\mu_e T_{\text{e}}}+\left[\eta_e k^2-\left(S_{\text{ioniz}|\varepsilon}-1\right)\left(\frac{2.4}{R_{\text{tube}}}\right)^2\right]\frac{\Upsilon_3}{\Upsilon_1}+\mu_{e|\varepsilon}k^2\frac{\Upsilon_1}{\Upsilon_2}\\
\Upsilon_1 &= k^2\frac{\varepsilon^2}{E_x^2}\left[\frac{D_e}{\mu_e T_{\text{e}}}\kappa_e+\chi_\varepsilon\left(\mu_\varepsilon+\mu_\varepsilon\mu_{\varepsilon|\varepsilon}-\eta_e\right)\right]+\frac{D_e}{\mu_e T_{\text{e}}}\left(\varepsilon_{\text{loss}|\varepsilon}+\mu_{e|\varepsilon}\right)+2\left(\mu_\varepsilon+\mu_\varepsilon\mu_{\varepsilon|\varepsilon}-\eta_e\right)\\
\Upsilon_2 &= k^4\frac{\varepsilon^4}{E_x^4}\kappa_e+k^2\frac{\varepsilon^2}{E_x^2}\left[2\kappa_e\left(\varepsilon_{\text{loss}|\varepsilon}+\mu_{e|\varepsilon}\right)+\left(\mu_\varepsilon+\mu_\varepsilon\mu_{\varepsilon|\varepsilon}-\eta_e\right)^2\right]+\left(\varepsilon_{\text{loss}|\varepsilon}+\mu_{e|\varepsilon}\right)^2\\
\Upsilon_3 &= k^4\frac{\varepsilon^4}{E_x^4}\kappa_e\chi_\varepsilon+k^2\frac{\varepsilon^2}{E_x^2}\left[\chi_\varepsilon\left(\varepsilon_{\text{loss}|\varepsilon}+\mu_{e|\varepsilon}\right)+2\kappa_e-\frac{D_e}{\mu_e T_{\text{e}}}\left(\mu_\varepsilon+\mu_\varepsilon\mu_{\varepsilon|\varepsilon}-\eta_e\right)\right]+2\left(\varepsilon_{\text{loss}|\varepsilon}+\mu_{e|\varepsilon}\right)
\end{aligned}
\tag{1}
$$

where, k is the wave number, E_x is the axial electric field, κ_e is the thermal conductivity of the electrons, η_e electron transport due to temperature gradient — Soret effect, χ_ε energy transport due to density gradient — Dufour effect, S_{ioniz} is the electron ionization source, $\varepsilon_{\text{loss}}$ is the electron energy loss. $S_{\text{ioniz}|\varepsilon}$, $\varepsilon_{\text{loss}|\varepsilon}$, $\mu_{e|\varepsilon}$, $\mu_{\varepsilon|\varepsilon}$ are log-log derivatives, e.g. $S_{ioniz|\varepsilon} = \partial \ln S_{ioniz,o}/\partial \ln \varepsilon_o$ where subscripts 'o' denotes unperturbed conditions.

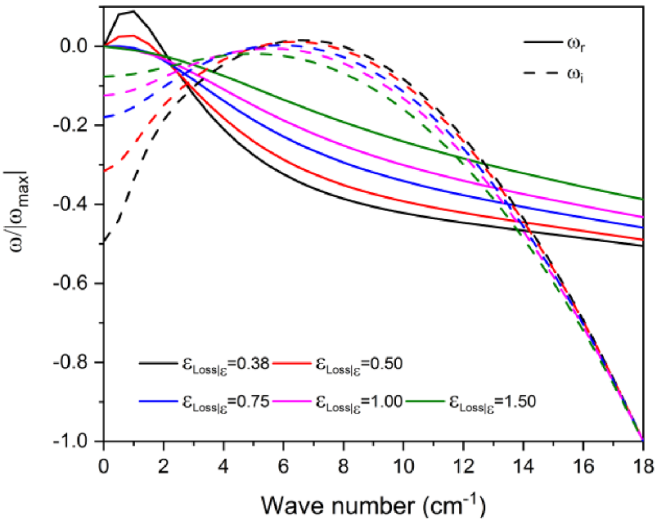

Figure 19. Calculated dispersion and amplification curves of wave instability in a low pressure nitrogen dc discharge for different values of $\varepsilon_{\text{loss}|\varepsilon}$ values. The positive column of the base case is utilized for the different parameter values in equation (1).

The calculated values of ω_r and ω_i are shown in figure 19 as a function of wave number for different $\varepsilon_{\text{loss}|\varepsilon}$ values. It should be noted that $\varepsilon_{\text{loss}|\varepsilon} = 0.38$ corresponds to the electron energy loss considering all the reactions in table 2. Both ω_r and ω_i have a strong dependence on $\varepsilon_{\text{loss}|\varepsilon}$ and can vary from positive to negative over the wave number range. For $\varepsilon_{loss|\varepsilon} = 0.38$, the dispersion curve has positive values at small wave numbers and decreases in a nonlinear fashion towards negative values at $\sim$3 cm^{-1}. As $\varepsilon_{\text{loss}|\varepsilon}$ increases, the dispersion curve remains negative for the rest of the wave numbers. The electron energy loss associated with the vibrational excitation process decreases the $\varepsilon_{\text{loss}|\varepsilon}$, the variation of the energy loss as a function of the mean energy. The different vibrational excitation spreads $\varepsilon_{\text{loss}|\varepsilon}$ progressively over the mean energy range. The energy loss associated with only dissociation and ionization results in a larger value of $\varepsilon_{\text{loss}|\varepsilon}$. The amplification curve has a weaker dependence on $\varepsilon_{\text{loss}|\varepsilon}$ and mostly remains negative for the entire range of wave numbers. However, for $\varepsilon_{\text{loss}|\varepsilon} = 0.38$, a slight positivity is evident, indicating the possibility of wave amplification. The presence of vibrationally excited states relaxes the plasma dependency on direct electron impact ionization and allows stepwise ionization to play a role. The stepwise ionization process requires lower threshold energy and is less sensitive to the electron energy making $\varepsilon_{\text{loss}|\varepsilon}$ to decrease [20].

6. Conclusions

A one-dimensional fluid model has been developed to simulate striations in nitrogen dc discharges at moderate gas pressures. The plasma model includes 22 species and 73 gas-phase reactions with multiple levels of vibrationally excited molecules. The simulations predicted standing striations with substantial oscillations of plasma density, electric field, electron temperature, vibrational temperature, and reaction rates. The modulation of the electron temperature occurred in the range of $\sim$1.60 – 1.66 eV. We found that the Dufour diffusivity is positive in this range of T_e, which implies stability with respect to thermodiffusion. The electron and ions' production and consumption rates in the striated plasma varied nonlinearly with the electron temperature: the consumption rate surpassed the formation rate until $\sim$1.63 eV. Our studies indicate that ionization and Dufour effect contribute to the formation of standing waves. Therefore, our results are consistent with the literature identifying Dufour diffusion as a potential instability source. Our results also indicate that the vibrational excitation of molecules and the ambipolar diffusion to the walls are essential in predicting the striation patterns in the considered range of discharge conditions. The study showed that the striations cease to exist without the vibrational excitation of molecules in the model. The linear stability analysis further confirmed that the electron energy loss associated with the vibrational excitation of nitrogen molecules could trigger instability and plasma stratification for the considered operating conditions.

Parametric studies helped determine the influence of discharge current on striation behavior. Operating in the 'abnormal' regime, the number of strata decreased with increasing current. No striations appeared at sufficiently high currents. Model predictions agreed favorably with experimental measurements. The predicted current–voltage characteristics agreed qualitatively well with the measured data but showed notable quantitative discrepancies. The model was able to capture the trend in the current density dependence of striations. The most substantial differences existed for the observed length of the Faraday dark space. The calculated length of the Faraday dark space was much shorter compared to the experimentally observed. These observed discrepancies are due to the well-known deficiencies of the fluid plasma model, which can not capture well the non-local kinetic effects in the cathode region of the abnormal discharges. It is expected that including a model for the fast electrons from the cathode sheath to describe the non-local ionization in the cathode region will improve the agreement with the experiments in future work. A better account for the radial transport of plasma species is expected to improve the model predictions as well.

Data availability statement

All data that support the findings of this study are included within the article (and any supplementary files).

Acknowledgments

TF was partially supported by the NSF project 1707282. VIK was partially supported by the NSF project OIA-1655280 and DOE project DE-SC0021391.

Appendix

Table A1. List of N_2 reactions considered in the EEDF calculation. Cross-section data are from [34].

#	Reaction
01	$e + N_2 \rightarrow e + N_2$
02	$e + N_2 \rightarrow e + N_{2,v=1}$
03	$e + N_2 \rightarrow e + N_{2,v=2}$
04	$e + N_2 \rightarrow e + N_{2,v=3}$
05	$e + N_2 \rightarrow e + N_{2,v=4}$
06	$e + N_2 \rightarrow e + N_{2,v=5}$
07	$e + N_2 \rightarrow e + N_{2,v=6}$
08	$e + N_2 \rightarrow e + N_{2,v=7}$
09	$e + N_2 \rightarrow e + N_{2,v=8}$
10	$e + N_2 \rightarrow e + N_{2,v=9}$
11	$e + N_2 \rightarrow e + N_{2,v=10}$
12	$e + N_2 \rightarrow e + N_{2,v=11}$
13	$e + N_2 \rightarrow e + N_{2,v=12}$
14	$e + N_2 \rightarrow e + N_{2,v=13}$
15	$e + N_2 \rightarrow e + N_{2,v=14}$
16	$e + N_2 \rightarrow e + N_{2,v=15}$
17	$e + N_2 \rightarrow e + N_2(A^3\Sigma, v = 0–4)$
18	$e + N_2 \rightarrow e + N_2(A^3\Sigma, v = 5–9)$
19	$e + N_2 \rightarrow e + N_2(B^3\Pi, v = 0–3)$
20	$e + N_2 \rightarrow e + N_2(W^3\Delta, v = 0–5)$
21	$e + N_2 \rightarrow e + N_2(A^3\Sigma, v = 10–21)$
22	$e + N_2 \rightarrow e + N_2(B^3\Pi, v = 4–16)$
23	$e + N_2 \rightarrow e + N_2(W^3\Delta, v = 6–10)$
24	$e + N_2 \rightarrow e + N_2(A^1\Pi, v = 0–3)$
25	$e + N_2 \rightarrow e + N_2(B!^3\Sigma, v = 0–6)$
26	$e + N_2 \rightarrow e + N_2(A!^1\Sigma, v = 0–6)$
27	$e + N_2 \rightarrow e + N_2(W^3\Delta, v = 11–19)$
28	$e + N_2 \rightarrow e + N_2(W^1\Delta, v = 0–5)$
29	$e + N_2 \rightarrow e + N_2(A^1\Pi, v = 4–15)$
30	$e + N_2 \rightarrow e + N_2(B!^3\Sigma, v = 7–18)$
31	$e + N_2 \rightarrow e + N_2(A!^1\Sigma, v = 7–19)$
32	$e + N_2 \rightarrow e + N_2(W^1\Delta, v = 6–18)$
33	$e + N_2 \rightarrow e + N_2(C^3\Pi, v = 0–4)$
34	$e + N_2 \rightarrow e + N_2(E^3\Sigma)$
35	$e + N_2 \rightarrow e + N_2(A!!^1\Sigma, v = 0–1)$
36	$e + N_2 \rightarrow e + N_2(B^1\Pi, v = 0–6)$
37	$e + N_2 \rightarrow e + N_2(C!^1\Sigma, v = 0–3)$
38	$e + N_2 \rightarrow e + N_2(G^3\Pi, v = 0–3)$
39	$e + N_2 \rightarrow e + N_2(C^{3\,1}\Pi, v = 0–3)$
40	$e + N_2 \rightarrow e + N_2(F^3\Pi, v = 0–3)$
41	$e + N_2 \rightarrow e + N_2(B!^1\Sigma, v = 0–10)$
42	$e + N_2 \rightarrow e + N_2(B^1\Pi, v = 7–14)$
43	$e + N_2 \rightarrow e + N_2(O^{3\,1}\Pi, v = 0–3)$
44	$e + N_2 \rightarrow e + N_2(B!^{3\,1}\Sigma, v = 10–H)$
45	$e + N_2 \rightarrow e + N_2(\text{sum singlets})$
46	$e + N_2 \rightarrow 2e + N_2^+$

Table A2. List of N reactions considered in the EEDF calculation. Cross-section data are from [35].

Process	Reaction
01	$e + N \rightarrow e + N$
02	$e + N \rightarrow e + N(2D)$
03	$e + N \rightarrow e + N(2P)$
04	$e + N \rightarrow 2e + N^+$

ORCID iDs

Malik M Tahiyat https://orcid.org/0000-0003-0024-9474
Jacob C Stephens https://orcid.org/0000-0002-2473-0329
Vladimir I Kolobov https://orcid.org/0000-0002-6197-3258
Tanvir I Farouk https://orcid.org/0000-0002-5579-0949

References

[1] Oleson N L and Cooper A W 1968 Moving striations *Adv. Electron. Electron. Phys.* **24** 155–278
[2] Kolobov V I 2006 Striations in rare gas plasmas *J. Phys. D: Appl. Phys.* **39** R487–506
[3] Golubovskii Y B, Nekuchaev V O and Skoblo A Y 2014 Advances in the study of striations in inert gases *Tech. Phys.* **59** 1787–800
[4] Kolobov V 2017 *Glow Discharges: Stratification, Encyclopedia of Plasma Technology* (Boca Raton FL: Taylor & Francis) pp 529–39
[5] Liu Y X, Schungel E, Korolov I, Donko Z, Wang Y N and Schulze J 2016 Experimental observation and computational analysis of striations in electrocnegative capacitively coupled radio-frequency plasmas *Phys. Rev. Lett.* **116** 255002
[6] Gudmundsson J T and Hecimovic A 2017 Foundations of DC plasma sources *Plasma Sources Sci. Technol.* **26** 123001–20
[7] Lisovskiy V A, Koval V A, Artushenko E P and Yegorenkov V D 2012 Validating the goldstein–wehner law for the stratified positive column of dc discharge in an undergraduate laboratory *Eur. J. Phys.* **33** 1537–45
[8] Pollard W, Suzuki P and Staack D 2014 Striations in high-pressure hydrogen microplasma *IEEE Trans. Plasma Sci.* **42** 2650–1
[9] Kawamura E, Lieberman M A and Lichtenberg A J 2017 Ionization instability induced striations in atmospheric pressure He/H2O RF and DC discharges *J. Phys. D: Appl. Phys.* **50** 145204
[10] Goldstein R A, Huerta M A and Nearing J C 1979 Stationary striations in an argon plasma as a bifurcation phenomenon *Phys. Fluids* **22** 231–40
[11] Pekarek L 1968 Ionization waves (striations) in a discharge plasma *Sov. Phys. Usp.* **11** 188
[12] Allis W P 1976 Review of glow discharge instabilities *Physica* B+C **82** 43–51
[13] Nighan W L and Wiegand W J 1974 Influence of negative-ion processes on steady-state properties and striations in molecular gas discharges *Phys. Rev.* A **10** 922–45
[14] Haas R A 1973 Plasma stability of electric discharges in molecular gases *Phys. Rev.* A **8** 1017–43
[15] Arslanbekov R R and Kolobov V I 2005 2D Simulations of striations in direct current glow discharges in argon *IEEE Trans. Plasma Sci.* **33** 354–5

[16] Golubovskii Y B, Skoblo A Y, Wilke C, Kozakov R V, Behnke J and Nekutchaev V O 2005 Kinetic resonances and stratification of the positive column of a discharge *Phys. Rev.* E **72** 026414

[17] Golubovskii Y B, Kolobov V I and Nekutchaev V O 2013 On electron bunching and stratification of glow discharges *Phys. Plasmas* **20** 101602

[18] Arslanbekov R R and Kolobov V I 2019 Advances in simulations of moving striations in DC discharges of noble gases *Phys. Plasmas* **26** 104501

[19] Désangles V, Raimbault J-L, Poyé A, Chabert P and Plihon N 2019 Pattern formation in low-pressure radio-frequency plasmas due to a transport instability *Phys. Rev. Lett.* **123** 265001

[20] Urbankova H and Rohlena K 1980 Electron thermal diffusion instability and standing striations in the plasma of a dc discharge in molecular gases *Czech. J. Phys.* B **30** 1227–35

[21] Mulders H C, Brok W J and Stoffels W W 2008 Striations in a low-pressure RF-driven argon plasma *IEEE Trans. Plasma Sci.* **36** 1380–1

[22] Iza F, Yang S, Kim H and Lee J K 2005 The mechanism of striation formation in plasma display panels *J. Appl. Phys.* **98** 043302

[23] Levko D and Raja L L 2017 magnetized direct current microdischarge i. effect of the gas pressure *J. Appl. Phys.* **121** 093302

[24] Golubovskii Y B, Maiorov V, Porokhova I and Behnke J 1999 On the non-local electron kinetics in spatially periodic striation-like fields *J. Phys. D: Appl. Phys.* **32** 1391

[25] Tsendin L 1995 Electron kinetics in non-uniform glow discharge plasmas *Plasma Sources Sci. Technol.* **4** 200

[26] Golubovskii Y, Valin S, Pelyukhova E, Nekuchaev V and Sigeneger F 2016 Discharge stratification in noble gases as convergence of electron phase trajectories to attractors *Phys. Plasmas* **23** 123518

[27] Levko D 2021 Electron kinetics in standing and moving striations in argon gas *Phys. Plasmas* **28** 013506

[28] Sigeneger F, Sukhinin G and Winkler R 2000 Kinetics of the electrons in striations of spherical glow discharges *Plasma Chem. Plasma Process.* **20** 87–110

[29] Mahamud R and Farouk T I 2016 Ion kinetics and self pulsing in DC microplasma discharges at atmospheric and higher pressure *J. Phys. D: Appl. Phys.* **49** 145202

[30] Farouk T, Farouk B, Staack D, Gutsol A and Fridman A 2006 Simulation of dc atmospheric pressure argon micro glow-discharge *Plasma Sources Sci. Technol.* **15** 676–88

[31] Kolobov V I, Arslanbekov R R, Levko D and Godyak V A 2020 Plasma stratification in radio-frequency discharges in argon gas *J. Phys. D: Appl. Phys.* **53** 25LT01

[32] Raizer Y P and Allen J E 1997 *Gas Discharge Physics* (Berlin: Springer)

[33] 2019 *COMSOL Multiphysics, Multiphysics Reference Guide for COMSOL 5.5* (Burlington, MA, USA) (https://www.comsol.com/support/knowledgebase/1223)

[34] Biagi S F FORTRAN Program, MAGBOLTZ v8.97 Oct 2012

[35] Alves L 2014 The IST-LISBON database on LXCat *J. Phys. Conf. Ser.* **565** 012007

[36] Kushner M 2021 Electron Impact Processes Hybrid Plasma Equipment Model personal communication

[37] Sakiyama Y, Graves D B, Chang H-W, Shimizu T and Morfill G E 2012 Plasma chemistry model of surface microdischarge in humid air and dynamics of reactive neutral species *J. Phys. D: Appl. Phys.* **45** 425201

[38] Van Gaens W and Bogaerts A 2013 Kinetic modelling for an atmospheric pressure argon plasma jet in humid air *J. Phys. D: Appl. Phys.* **46** 275201

[39] Peterson J *et al* 1998 Dissociative recombination and excitation of N 2+: cross sections and product branching ratios *J. Chem. Phys.* **108** 1978–88

[40] Sommerer T J and Kushner M J 1992 Numerical investigation of the kinetics and chemistry of rf glow discharge plasmas sustained in He, N2, O2, He/N2/O2, He/CF4/O2, and SiH4/NH3 using a monte carlo-fluid hybrid model *J. Appl. Phys.* **71** 1654–73

[41] Appleton J, Steinberg M and Liquornik D 1968 Shock-tube study of nitrogen dissociation using vacuum-ultraviolet light absorption *J. Chem. Phys.* **48** 599–608

[42] Billing G D and Fisher E 1979 VV and VT rate coefficients in N2 by a quantum-classical model *Chem. Phys.* **43** 395–401

[43] Ahn T, Adamovich I V and Lempert W R 2004 Determination of nitrogen V–V transfer rates by stimulated Raman pumping *Chem. Phys.* **298** 233–40

[44] Biagi S F 1999 Monte carlo simulation of electron drift and diffusion in counting gases under the influence of electic and magnetic field *Nucl. Instrum. Methods Phys. Res.* A **421** 234–40

[45] Farouk T, Farouk B, Gutsol A and Fridman A 2008 Atmospheric pressure methane–hydrogen dc micro-glow discharge for thin film deposition *J. Phys. D: Appl. Phys.* **41** 175202

[46] Farouk T, Farouk B and Fridman A 2010 Computational studies of atmospheric pressure methane-hydrogen DC micro glow discharges *IEEE Trans. Plasma Sci.* **38** 73–85

[47] White R D, Robson R E, Schmidt B and Morrison M A 2003 Is the classical two-term approximation of electron kinetic theory satisfactory for swarms and plasmas? *J. Phys. D: Appl. Phys.* **36** 3125

[48] Pitchford L, ONeil S and Rumble J 1981 Extended boltzmann analysis of electron swarm experiments *Phys. Rev.* A **23** 294

[49] Pitchford L and Phelps A 1982 Comparative calculations of electron-swarm properties in N 2 at moderate E N values *Phys. Rev.* A **25** 540

[50] Dujko S, Markosyan A, White R and Ebert U 2013 High-order fluid model for streamer discharges: I. Derivation of model and transport data *J. Phys. D: Appl. Phys.* **46** 475202

[51] Markosyan A, Dujko S and Ebert U 2013 High-order fluid model for streamer discharges: II. Numerical solution and investigation of planar fronts *J. Phys. D: Appl. Phys.* **46** 475203

[52] Stephens J 2018 A multi-term Boltzmann equation benchmark of electron-argon cross-sections for use in low temperature plasma models *J. Phys. D: Appl. Phys.* **51** 125203

[53] Hagelaar G and Pitchford L 2005 Solving the Boltzmann equation to obtain electron transport coefficients and rate coefficients for fluid models *Plasma Sources Sci. Technol.* **14** 722

[54] Cacciatore M, Capitelli M and Gorse C 1982 Non-equilibrium dissociation and ionization of nitrogen in electrical discharges: the role of electronic collisions from vibrationally excited molecules *Chem. Phys.* **66** 141–51

[55] Boeuf J and Kunhardt E 1986 Energy balance in a nonequilibrium weakly ionized nitrogen discharge *J. Appl. Phys.* **60** 915–23

[56] Yao J, Yuan C, Eliseev S, Kudryavtsev A and Zhou Z 2020 Longitudinal structure and plasma parameters of an entire DC glow discharge as obtained using a 1D fluid-based model with non-local ionization *Plasma Sources Sci. Technol.* **29** 075003